

Heavy Quark Photoproduction in Ultra-peripheral Heavy Ion Collisions

Spencer R. Klein¹, Joakim Nystrand², and Ramona Vogt^{1,3}

¹*Lawrence Berkeley National Laboratory, Berkeley, CA 94720*

²*Department of Physics, Lund University, Lund SE-22100, Sweden*

³*Physics Department, University of California, Davis, CA 95616*

Abstract

Heavy quarks are copiously produced in ultra-peripheral heavy ion collisions. In the strong electromagnetic fields, $c\bar{c}$ and $b\bar{b}$ are produced by photonuclear and two-photon interactions. Hadroproduction can also occur in grazing interactions. We calculate the total cross sections and the quark transverse momentum and rapidity distributions, as well as the $Q\bar{Q}$ invariant mass spectra from the three production channels. We consider AA and pA collisions at the Relativistic Heavy Ion Collider and the Large Hadron Collider. We discuss techniques for separating the three processes and describe how the AA to pA production ratios might be measured accurately enough to study nuclear shadowing.

I. INTRODUCTION

In ultra-peripheral heavy ion collisions, heavy quarks can be produced in electromagnetic or hadronic interactions. Electromagnetic production occurs through strong electromagnetic fields which can interact with a target nucleus in the opposing beam (photoproduction) or with the electromagnetic field of the opposing beam (two-photon reactions) and produce hadronic final states, including heavy quark pairs. Hadroproduction of heavy quark pairs is also possible in grazing interactions. Since photon emission is coherent over the entire nucleus and because the photon is colorless, the three channels can be distinguished by the presence of zero, one or two rapidity gaps in the events and by whether or not the nuclei dissociate.

Many types of ultra-peripheral collisions have been considered [1]. Photonuclear interaction studies have included Coulomb dissociation [2] and coherent vector meson production [3,4]. Final states studied in two-photon interactions have included production of lepton pairs [5], single mesons and meson pairs [6] as well as production of the

Higgs boson and other exotica [7]. Although the list of experimentally observed channels is currently short, as RHIC gears up new results should come quickly and measurements of heavy quark production in ultra-peripheral collisions may not be too far off.

We build on previous calculations of heavy quark photoproduction [8–10] and two-photon production [11] in heavy ion collisions. For the first time, we consider resolved photon processes. We use modern parton distribution functions along with up-to-date accelerator species and luminosities. We also consider hadroproduction in grazing collisions and compare the three channels. Finally, since useful measurements of shadowing will require high accuracy, we consider the uncertainties inherent in these calculations and methods to control them.

We will compare the total cross sections, heavy quark transverse momentum, p_T , and rapidity, y , distributions, and the $Q\bar{Q}$ pair invariant mass, M , distributions in all three channels. We also discuss pA collisions to see how a comparison of photoproduction in AA (γA) and pA (effectively γp) can be used to study nuclear effects on the parton distribution functions (shadowing).

For consistency, we will use parallel approaches to all three calculations with the same quark mass, parton distribution and QCD scale. For the charm quark mass, m_c , this is somewhat problematic because studies of different production channels seem to prefer different values. Hadroproduction calculations have typically best fit the data with a relatively light m_c , $\sim 1.2 - 1.4$ GeV [12], while photoproduction studies have generally favored higher values, $1.5 - 1.8$ GeV [13,14]. The limited two-photon data favors an intermediate value, around 1.6 GeV [15,16]. For the bottom quark, the typical mass range considered is $4.5 - 5.0$ GeV. Hadroproduction calculations with $m_b = 4.75$ GeV underpredict the $b\bar{b}$ cross section observed in 1.8 TeV $p\bar{p}$ collisions [17], suggesting that a smaller mass might be preferred [17]. Some exotic b production mechanisms have been suggested to explain the excess [18,19]. Lattice studies suggest lower c and b quark masses, $1.1 - 1.4$ GeV for charm and $4.1 - 4.4$ GeV for bottom (the pole masses are somewhat higher) [20]. We use $m_c = 1.2$ GeV and $m_b = 4.75$ GeV throughout this paper but we will also discuss the effect of varying the mass and scale. The QCD scale entering the running coupling constant, $\alpha_s(Q^2)$, and the parton distribution functions are proportional to the transverse masses, $Q^2 = 4m_T^2$ for charm and m_T^2 for bottom [12].

Table I gives recent estimates of nucleon-nucleon center of mass energies, \sqrt{S} , and luminosities for AA and pA collisions at RHIC [21] and the LHC [22,23]. The LHC luminosities assume that two experiments take data and that there is a 125 ns bunch spacing. At RHIC, the pA energies are the same as the AA energies while the luminosities are taken to be the geometric mean of the AA and pp luminosities ($\mathcal{L}_{pp} = 1.4 \times 10^{31}$ cm⁻² s⁻¹). There is also the possibility of pA collisions at the LHC. However, at the LHC, the proton and the ion must have the same magnetic rigidity. Because protons and ions have different charge to mass ratios, they have different per nucleon energies and the center of mass is no longer at rest in the lab. These pA collisions are then at somewhat higher per nucleon energies than the corresponding AA collisions. At the

LHC, the pA collision rates can exceed 200 kHz although some experiments may need to run at a lower luminosity. Because RHIC is a dedicated heavy ion accelerator, it is likely to run a wider variety of beams than the LHC. At RHIC, dA collisions may be an alternative or supplement to pA . Except for the different initial isospin, most of the pA discussion should also hold for dA because shadowing is small in deuterium.

Section II discusses photoproduction of heavy quarks in AA and pA collisions. Section III covers hadroproduction in peripheral AA and minimum bias pA collisions. Section IV considers $\gamma\gamma \rightarrow Q\bar{Q}$ production. Section V compares our results for the three channels while section VI is dedicated to a discussion of how to disentangle the production channels experimentally. In section VII, we draw our conclusions.

II. PHOTOPRODUCTION

Photoproduction of heavy quarks occurs when a photon emitted from one nucleus fuses with a gluon from the other nucleus, forming a $Q\bar{Q}$ pair [8,9,24] (“direct” production), as in Fig. 1(a). The photon can also fluctuate into a state with multiple $q\bar{q}$ pairs and gluons, *i.e.* $|n(q\bar{q})m(g)\rangle$. One of these photon components can interact with a quark or gluon from the target nucleus (“resolved” production), as in Figs. 1(b)-(d) [25]. The photon components are described by parton densities similar to those used for protons except that no useful momentum sum rule applies to the photon [26].

At leading order (LO), the partonic cross section of the direct contribution is proportional to $\alpha\alpha_s(Q^2)e_Q^2$, where $\alpha_s(Q^2)$ is the strong coupling constant, $\alpha = e^2/\hbar c$ is the electromagnetic coupling constant, and e_Q is the quark charge, $e_c = 2/3$ and $e_b = -1/3$. The resolved partonic cross section is proportional to $\alpha_s^2(Q^2)$. Even though the resolved partonic cross sections are larger than the direct partonic cross section, the smaller flux of quarks and gluons from the photon suggests that the resolved contribution should be smaller than the direct component.

The cross sections are calculated using the Weizsäcker-Williams virtual photon flux, modern parameterizations of the target gluon and quark distributions and the LO partonic cross sections. Newer parton distributions are considerably softer than the flat, scaling parameterizations used earlier [8,9]. We require that the photoproduction not be accompanied by hadronic interactions [8,9]. This could be done by restricting the impact parameter, b , to greater than twice the nuclear radius, R_A . Here we weight the b -dependent photoproduction probability by the b -dependent hadronic non-interaction probability.

Direct $Q\bar{Q}$ pairs are produced in the reaction $\gamma(k) + N(P_2) \rightarrow Q(p_1) + \bar{Q}(p_2) + X$ where k is the four momentum of the photon emitted from the virtual photon field of the projectile nucleus, P_2 is the four momentum of the interacting nucleon N in ion A ,

and p_1 and p_2 are the four momenta of the produced Q and \bar{Q} . The photons are almost real. Their slight virtuality, $|q^2| < (\hbar c/R_A)^2$, is neglected.

On the parton level, the photon-gluon fusion reaction is $\gamma(k) + g(x_2 P_2) \rightarrow Q(p_1) + \bar{Q}(p_2)$ where x_2 is the fraction of the target momentum carried by the gluon. The LO $Q\bar{Q}$ photoproduction cross section for quarks with mass m_Q is [27]

$$s^2 \frac{d^2 \sigma_{\gamma g}}{dt_1 du_1} = \pi \alpha_s(Q^2) \alpha e_Q^2 B_{\text{QED}}(s, t_1, u_1) \delta(s + t_1 + u_1) \quad (1)$$

where

$$B_{\text{QED}}(s, t_1, u_1) = \frac{t_1}{u_1} + \frac{u_1}{t_1} + \frac{4m_Q^2 s}{t_1 u_1} \left[1 - \frac{m_Q^2 s}{t_1 u_1} \right]. \quad (2)$$

Here $\alpha_s(Q^2)$ is evaluated to one loop at scale Q^2 . The partonic invariants, s , t_1 , and u_1 , are defined as $s = (k + x_2 P_2)^2$, $t_1 = (k - p_1)^2 - m_Q^2 = (x_2 P_2 - p_2)^2 - m_Q^2$, and $u_1 = (x_2 P_2 - p_1)^2 - m_Q^2 = (k - p_2)^2 - m_Q^2$. In this case, $s = 4k\gamma_L x_2 m_p$ where γ_L is the Lorentz boost of a single beam and m_p is the proton mass. Since k ranges over a continuum of energies up to $E_{\text{beam}} = \gamma_L m_p$, we define $x_1 = k/P_1$ analogous to the parton momentum fraction where P_1 is the nucleon four momentum. For a detected quark in a nucleon-nucleon collision, the hadronic invariants are then $S = (P_1 + P_2)^2$, $T_1 = (P_2 - p_1)^2 - m_Q^2$, and $U_1 = (P_1 - p_1)^2 - m_Q^2$.

We label the quark rapidity as y_1 and the antiquark rapidity as y_2 . The quark rapidity is related to the invariant T_1 by $T_1 = -\sqrt{S} m_T e^{-y_1}$ where $m_T = \sqrt{p_T^2 + m_Q^2}$. The invariant mass of the pair can be determined if both the Q and \bar{Q} are detected. The square of the invariant mass, $M^2 = s = 2m_T^2(1 + \cosh(y_1 - y_2))$, is the partonic center of mass energy squared. The minimum photon momentum necessary to produce a $Q\bar{Q}$ pair is $k_{\text{min}} = M^2/4\gamma_L m_p$. At LO, $x_2 = (m_T/\sqrt{S})(e^{y_1} + e^{y_2})$ and $x_1 = (m_T/\sqrt{S})(e^{-y_1} + e^{-y_2})$. We calculate x_1 and x_2 as in an NN collision and then determine the flux in the lab frame for $k = x_1 \gamma_L m_p$, equivalent to the center of mass frame in a collider. The photon flux is exponentially suppressed for $k > \gamma_L \hbar c/R_A$, corresponding to a momentum fraction $x_1 > \hbar c/m_p R_A$. The maximum γN center of mass energy, $\sqrt{S_{\gamma N}}$, is much lower than the hadronic \sqrt{S} . Note that $\sqrt{S_{\gamma N}} = W_{\gamma N}$, the typical notation for HERA. For consistency, we use \sqrt{S} notation for all three processes.

The cross section for direct photon-nucleon heavy quark photoproduction is obtained by convoluting Eq. (1) with the photon flux and the gluon distribution in the nucleus and integrating over k and x_2 ,

$$S^2 \frac{d^2 \sigma_{\gamma A \rightarrow Q\bar{Q}X}^{\text{dir}}}{dT_1 dU_1 d^2 b} = 2 \int dz \int_{k_{\text{min}}}^{\infty} dk \frac{d^3 N_{\gamma}}{dk d^2 b} \int_{x_{2,\text{min}}}^1 \frac{dx_2}{x_2} F_g^A(x_2, Q^2, \vec{b}, z) s^2 \frac{d^2 \sigma_{\gamma g}}{dt_1 du_1}, \quad (3)$$

where $d^3 N_\gamma/dkd^2b$ is the differential photon flux from one nucleus (our final results will be integrated over $b > 2R_A$) and z is the longitudinal distance. The factor of two in Eq. (3) arises because both nuclei emit photons and thus serve as targets. The incoherence of heavy quark production eliminates interference between the two production sources [28]. Four-momentum conservation gives $x_{2\min} = -U_1/(S + T_1)$ in terms of the nucleon-nucleon invariants. The equivalent hadronic invariants can be defined for photon four momentum k as $S_{\gamma N} = (k + P_2)^2$, $T_{1,\gamma N} = (P_2 - p_1)^2 - m_Q^2$, and $U_{1,\gamma N} = (k - p_1)^2 - m_Q^2$ [29]. The partonic and equivalent hadronic invariants for fixed k are related by $s = x_2 S_{\gamma N}$, $t_1 = U_{1,\gamma N}$, and $u_1 = x_2 T_{1,\gamma N}$.

We now turn to the resolved (hadronic) contribution to the photoproduction cross section. The hadronic reaction, $\gamma N \rightarrow Q\bar{Q}X$, is unchanged, but now, prior to the interaction with the nucleon, the photon splits into a color singlet state with some number of $q\bar{q}$ pairs and gluons. There are a few photon parton distributions available [30–34]. None of them can be definitively ruled out by the existing data on the photon structure function [35,36]. As expected, $F_q^\gamma(x, Q^2) = F_q^\gamma(x, Q^2)$ flavor by flavor because there are no “valence” quarks in the photon. The gluon distribution in the photon is less well known. We use the GRV LO set [30]. Its gluon distribution is similar to most of the other available sets [31,33,34]. Only the LAC1 set [32] has a higher low- x gluon density, up to an order of magnitude larger than the others.

On the parton level, the resolved LO reactions are $g(xk) + g(x_2P_2) \rightarrow Q(p_1) + \bar{Q}(p_2)$ and $q(xk) + \bar{q}(x_2P_2) \rightarrow Q(p_1) + \bar{Q}(p_2)$ where x is the fraction of the photon momentum carried by the parton. The LO diagrams for resolved photoproduction, shown in Fig. 1(b)-(d), are the same as for hadroproduction except that one parton source is a photon rather than a nucleon. The LO partonic cross sections are [37]

$$\hat{s}^2 \frac{d^2 \sigma_{q\bar{q}}}{d\hat{t}_1 d\hat{u}_1} = \pi \alpha_s^2(Q^2) \frac{4}{9} \left(\frac{\hat{t}_1^2 + \hat{u}_1^2}{\hat{s}^2} + \frac{2m_Q^2}{\hat{s}} \right) \delta(\hat{s} + \hat{t}_1 + \hat{u}_1), \quad (4)$$

$$\hat{s}^2 \frac{d^2 \sigma_{gg}}{d\hat{t}_1 d\hat{u}_1} = \frac{\pi \alpha_s^2(Q^2)}{16} B_{\text{QED}}(\hat{s}, \hat{t}_1, \hat{u}_1) \left[3 \left(1 - \frac{2\hat{t}_1 \hat{u}_1}{\hat{s}^2} \right) - \frac{1}{3} \right] \delta(\hat{s} + \hat{t}_1 + \hat{u}_1), \quad (5)$$

where $\hat{s} = (xk + x_2P_2)^2$, $\hat{t}_1 = (xk - p_1)^2 - m_Q^2$, and $\hat{u}_1 = (x_2P_2 - p_1)^2 - m_Q^2$. The gg partonic cross section, Eq. (5), is proportional to the photon-gluon fusion cross section, Eq. (1), with an additional factor for the non-Abelian three-gluon vertex. The $q\bar{q}$ annihilation cross section has a different structure because it is an s -channel process with gluon exchange between the $q\bar{q}$ and $Q\bar{Q}$ vertices. The gg reactions are shown in Figs. 1(b)-(c); Fig. 1(c) is the non-Abelian contribution. The $q\bar{q}$ diagram is shown in Fig. 1(d). Modulo the additional factor in the gg cross section, the resolved partonic photoproduction cross sections are a factor $\alpha_s(Q^2)/\alpha e_Q^2$ larger than the direct, γg , partonic photoproduction cross sections. Despite this, the resolved component is still smaller than the direct component.

The cross section for resolved photoproduction is

$$\begin{aligned}
S^2 \frac{d^2 \sigma_{\gamma A \rightarrow Q \bar{Q} X}^{\text{res}}}{dT_1 dU_1 d^2 b} &= 2 \int dz \int_{k_{\min}}^{\infty} \frac{dk}{k} \frac{d^3 N_{\gamma}}{dk db^2} \int_{k_{\min}/k}^1 \frac{dx}{x} \int_{x_{2\min}}^1 \frac{dx_2}{x_2} \\
&\times \left[F_g^{\gamma}(x, Q^2) F_g^A(x_2, Q^2, \vec{b}, z) \hat{s}^2 \frac{d^2 \sigma_{gg}}{d\hat{t}_1 d\hat{u}_1} \right. \\
&\left. + \sum_{q=u,d,s} F_q^{\gamma}(x, Q^2) \left\{ F_q^A(x_2, Q^2, \vec{b}, z) + F_{\bar{q}}^A(x_2, Q^2, \vec{b}, z) \right\} \hat{s}^2 \frac{d^2 \sigma_{q\bar{q}}}{d\hat{t}_1 d\hat{u}_1} \right], \quad (6)
\end{aligned}$$

where k_{\min} is defined as before. Since k is typically larger in resolved than direct photoproduction, the average photon flux is lower in the resolved contribution.

The nuclear parton densities $F_i^A(x, Q^2, \vec{b}, z)$ in Eqs. (3) and (6) can be factorized into x and Q^2 independent nuclear density distributions, position and nuclear-number independent nucleon parton densities, and a shadowing function $S^i(A, x, Q^2, \vec{b}, z)$ that describes the modification of the nuclear parton distributions in position and momentum space. Then [38–42]

$$F_i^A(x, Q^2, \vec{b}, z) = \rho_A(\vec{b}, z) S^i(A, x, Q^2, \vec{b}, z) f_i^N(x, Q^2) \quad (7)$$

where $f_i^N(x, Q^2)$ is the parton density in the nucleon. We evaluate the MRST LO parton distributions [43] at $Q^2 = a^2 m_f^2$, where $a = 2$ for charm and 1 for bottom. In the absence of nuclear modifications, $S^i(A, x, Q^2, \vec{b}, z) \equiv 1$. The nuclear density distribution, $\rho_A(\vec{b}, z)$, is a Woods-Saxon shape with parameters determined from electron scattering data [44]. Although most models of shadowing predict a dependence on the parton position in the nucleus, in this photoproduction calculation we neglect any impact parameter dependence. Then the position dependence drops out of S^i . We employ the EKS98 shadowing parameterization [45], available in PDFLIB [35] for $S^i \neq 1$.

The full photoproduction cross section is the sum of the direct and resolved contributions [13],

$$S^2 \frac{d^2 \sigma_{\gamma A \rightarrow Q \bar{Q} X}}{dT_1 dU_1 d^2 b} = S^2 \frac{d^2 \sigma_{\gamma A \rightarrow Q \bar{Q} X}^{\text{dir}}}{dT_1 dU_1 d^2 b} + S^2 \frac{d^2 \sigma_{\gamma A \rightarrow Q \bar{Q} X}^{\text{res}}}{dT_1 dU_1 d^2 b}. \quad (8)$$

The total cross section is the integral over impact parameter and the hadronic invariants T_1 and U_1 ,

$$\sigma_{\gamma A \rightarrow Q \bar{Q} X} = \int dT_1 dU_1 d^2 b \frac{d^2 \sigma_{\gamma A \rightarrow Q \bar{Q} X}}{dT_1 dU_1 d^2 b}. \quad (9)$$

When $S^i = 1$, the impact-parameter integrated cross section in Eq. (9) scales with A . Including shadowing makes the dependence on A nonlinear.

The photon flux is given by the Weizsäcker-Williams method. The flux from a charge Z nucleus a distance r away is

$$\frac{d^3 N_\gamma}{dk d^2 r} = \frac{Z^2 \alpha w^2}{\pi^2 k r^2} \left[K_1^2(w) + \frac{1}{\gamma_L^2} K_0^2(w) \right] \quad (10)$$

where $w = kr/\gamma_L$ and $K_0(w)$ and $K_1(w)$ are modified Bessel functions. The photon flux decreases exponentially above a cutoff energy determined by the size of the nucleus. In the lab frame, the cutoff is $k_{\max} \approx \gamma_L \hbar c / R_A$. In the rest frame of the target nucleus, the cutoff is boosted to $E_{\max} = (2\gamma_L^2 - 1) \hbar c / R_A$. Table II shows the beam energies, E_{beam} , Lorentz factors, γ_L , k_{\max} , and E_{\max} , as well as the corresponding maximum center of mass energy, $\sqrt{S_{\max}} = \sqrt{2E_{\max} m_p}$, for single photon interactions with protons, $\gamma p \rightarrow Q\bar{Q}$ [46]. At the LHC, the energies are high enough for $t\bar{t}$ photoproduction [10].

The total photon flux striking the target nucleus is the integral of Eq. (10) over the transverse area of the target for all impact parameters subject to the constraint that the two nuclei do not interact hadronically [3]. This must be calculated numerically. However, a reasonable analytic approximation for AA collisions is given by the photon flux integrated over radii $r > 2R_A$. The analytic photon flux is

$$\frac{dN_\gamma}{dk} = \frac{2Z^2 \alpha}{\pi k} \left[w_R^{AA} K_0(w_R^{AA}) K_1(w_R^{AA}) - \frac{(w_R^{AA})^2}{2} (K_1^2(w_R^{AA}) - K_0^2(w_R^{AA})) \right] \quad (11)$$

where $w_R^{AA} = 2kR_A/\gamma_L$. We use the more accurate numerical calculations here. The difference between the numerical and analytic expressions is typically less than 15%, except for photon energies near the cutoff. The analytical and numerical photon fluxes differ most for $b\bar{b}$ production at RHIC.

The photoproduction distributions are shown in Figs. 2-5 for the largest nuclei at each energy, gold for RHIC and lead for LHC. Since $\sqrt{S_{\max}}$ is close to the $b\bar{b}$ production threshold for iodine and gold beams at RHIC, the p_T and mass distributions for these nuclei are narrower than those with oxygen and silicon beams. The direct photoproduction results are reduced by a factor of two on the figures to separate them from the total. There are two curves for each contribution, one without shadowing, $S^i = 1$, and one with homogeneous nuclear shadowing, $S^i = \text{EKS98}$. When the effects of shadowing are small, the curves are indistinguishable.

Shadowing has the largest effect on the rapidity distributions in Figs. 2(b)-5(b). In these calculations, the photon is emitted from the nucleus coming from positive rapidity. Then $y_1 < 0$ corresponds to $k < \gamma_L x_2 m_p$ in the center of mass (lab) frame. If the photon emitter and target nucleus are interchanged, the resulting unshadowed rapidity distribution, $S^i = 1$, is the mirror image of these distributions around $y_1 = 0$. The Q and \bar{Q} distributions are asymmetric around $y_1 = 0$. The resolved contribution is largest at rapidities where the photon momentum is small. The resolved rapidity distributions

are narrower and shifted to larger negative rapidity than the direct contribution. The average mass and transverse momentum for the resolved component are smaller than for the direct ones. The total heavy quark rapidity distributions are the sum of the displayed results with their mirror images when both nuclei emit photons. This factor of two is included in the transverse momentum and invariant mass distributions.

The impact-parameter integrated total direct and resolved photoproduction cross sections are given in Table III for charm and Table IV for bottom. The difference between the $S^i = 1$ and $S^i = \text{EKS98}$ calculations is due to shadowing. The change is about 10% for $c\bar{c}$ with gold at RHIC, rising to 20% for $c\bar{c}$ with lead at the LHC. For $b\bar{b}$, the shadowing effect is smaller, about 5%. By selecting charm production in a limited rapidity and p_T range, it would be possible to enhance the effect of shadowing slightly but the 10% and 20% effects at RHIC and the LHC are useful benchmarks of the accuracy needed for a meaningful measurement.

The cross sections vary by orders of magnitude between the lightest and heaviest targets, primarily due to the changing Z^2 . At RHIC, $(Z_{\text{Au}}/Z_{\text{O}})^2$ is almost exactly the ratio of the $b\bar{b}$ production cross sections. For $b\bar{b}$ production at the LHC, the lead to oxygen cross section ratio is ~ 60 , less than $(Z_{\text{Pb}}/Z_{\text{O}})^2$.

After adjustment for different parton distributions, quark masses, beam energies and species as well as the resolved contributions, the photoproduction results are comparable with previous studies. The direct $c\bar{c}$ cross sections in Table III are almost identical to those found by Baron and Baur [8], despite significant differences in gluon structure function and quark masses (*e.g.* $m_c = 1.74$ GeV in Ref. [8] rather than $m_c = 1.2$ GeV). The quark mass difference can be compensated by the newer parton distributions since the low- x MRST gluon density is much higher than that of the older Duke-Owens parton distributions used by Baron and Baur. Our $b\bar{b}$ cross section is about three times higher than Greiner *et al.* [9,47] at the same invariant mass although they use a smaller b quark mass, 4.5 GeV, due to the larger low- x MRST gluon distribution.

On the other hand, nonperturbative QCD calculations of direct photoproduction can yield very different rates. A colored glass model predicts $Q\bar{Q}$ production cross sections in Pb+Pb collisions at the LHC of 800 mb for $c\bar{c}$ and 100 mb for $b\bar{b}$ [48], about half the perturbative $c\bar{c}$ cross section but 140 times the $b\bar{b}$ cross section. The ratio of charm to bottom cross sections in this formulation is extraordinarily small compared to the perturbative results in Tables III and IV.

We now discuss the resolved rates. At RHIC the $c\bar{c}$ and $b\bar{b}$ resolved contributions are ~ 2 and 6% of the total. The contribution is small because the available γp energy is relatively close to threshold: the resolved center of mass energy is smaller than $\sqrt{S_{\text{max}}}$. At the LHC, the resolved contributions are ~ 15 and 20% of the total charm and bottom photoproduction cross sections respectively, comparable to the shadowing effect. Interestingly, the resolved $q\bar{q}$ component is considerably greater than $q\bar{q}$ annihilation in hadroproduction because, like the valence quark distributions of the proton, the photon

quark and antiquark distributions peak at large x . However, the peak of the photon quark distribution is at higher x than in the proton. These large photon momentum fractions increase the $q\bar{q}$ contribution near threshold. The total $c\bar{c}$ resolved cross section at RHIC is $(35 - 50)\%$ $q\bar{q}$ while the $b\bar{b}$ resolved contribution is $(80 - 90)\%$ $q\bar{q}$. The relative resolved contribution remains larger than $q\bar{q}$ annihilation in hadroproduction at the LHC where the $q\bar{q}$ contribution to the hadroproduction cross section is 4% for charm and 10% for bottom. The LAC1 gluon distribution [32] predicts a considerably larger resolved contribution with a smaller relative $q\bar{q}$ contribution.

At fixed target energies, near threshold, the resolved component of charm photoproduction is relatively unimportant [51]. However, at higher γp energies such as those at HERA, the resolved component becomes important. RHIC is an intermediate case, with an average γp energy less than 1/5 of that at HERA. We find that, at RHIC, the resolved component is a $(2 - 6)\%$ effect. At the LHC, where the energies are generally higher than at HERA, it is $(15 - 20)\%$ of the total cross section, concentrated at large rapidities. As was previously mentioned, much early photoproduction data favors heavier quark masses, 1.5 – 1.8 GeV, although newer HERA results are ambiguous [52]. Because we use a lower m_c , our cross sections are higher than a direct comparison to HERA would indicate. Changing m_c affects the overall cross section and the quark p_T spectrum for $p_T < 5$ GeV [13].

As is typically done, we include all $Q\bar{Q}$ pairs in the total cross sections and rates even though some of these pairs have masses below the $H\bar{H}$ threshold where $H\bar{H} \equiv D\bar{D}, B\bar{B}$. Photoproduction is an inclusive process; accompanying particles can combine with the Q and \bar{Q} , allowing the pairs with $M < 2m_H$ to hadronize. We assume the hadronization process does not affect the rate. Including all pairs in the total cross section is presumably an even safer assumption for hadroproduction because there are more accompanying particles. On the other hand, $\gamma\gamma$ interactions should have no additional particles since the interaction is purely electromagnetic and occurs away from the nuclei in free space. Section IV will discuss this in more detail.

One way to avoid some uncertainties due to higher order corrections is to measure shadowing by comparing the pA and AA photoproduction cross sections at equal photon energies since the parameter dependence cancels in the ratio $\sigma(AA)/\sigma(pA)$. In the equal speed system, equal photon energies correspond to the same final-state rapidities. In pA collisions, the photon almost always comes from the nucleus due to its stronger field. Thus the pA rates depend on the free proton gluon distribution. The photon fluxes are different for pA and AA because the minimum radii used to determine ω_R are different: $2R_A$ in AA compared to $R_A + r_p$ in pA where r_p is the proton radius. There are a number of ways to define the proton radius. We use the hadronic radius, $r_p \approx 0.6$ fm, determined from photoproduction data [53]. As we will show, our results are not very sensitive to r_p .

In a detailed calculation, the hadronic interaction probability near the minimum radius depends on the matter distribution in the nucleus. Our calculations use Woods-

Saxon distributions with parameters fit to electron scattering data. This data is quite accurate. However, electron scattering is only sensitive to the charge distribution in the nucleus. Recent measurements indicate that the neutron and proton distributions differ in nuclei [54]. This uncertainty in the matter distribution is likely to limit the photon flux determination.

The uncertainty in the photon flux can be reduced by calibrating it with other measurements. Further studies of the matter distributions in nuclei [54] and the total ion-ion cross sections, as well as comparisons with known photoproduction and two-photon processes, can help pin down the photon flux. For example, the cross section for $\gamma p \rightarrow \rho p$ is known to 10% from measurements at HERA [53]. The $\gamma A \rightarrow VA$ data are limited to energies lower than but still comparable to those available at RHIC. A combination of lower energy RHIC data and a judicious extrapolation could fix the calibration. Studies of well known two-photon processes, like lepton production, can also help refine the determination of the photon flux. With these checks, it should be possible to understand the photon flux in pA relative to AA to better than 10%, good enough for a useful shadowing measurement.

Our pA results are calculated in the equal-speed frame. This is appropriate for RHIC where \sqrt{S} is the same in pA and AA interactions. At the LHC, the proton and nuclear beams must have the same magnetic rigidity and, hence, different velocities and per-nucleon energies. At the LHC, the equal-speed frame is moving in the laboratory frame so that the maximum pA energy is larger than the AA energy. The γ_L and \sqrt{S} given for pA at the LHC in Tables I and II are those of the equal-speed system. The pA total cross sections for $Q\bar{Q}$ production are given in Table V.

It is easy to compare pA and AA results at RHIC. For $S^i = 1$, the only difference is in the impact parameter range: $b > 2R_A$ in AA compared to $b > R_A + r_p$ in pA . We compare the numerical AA results presented in Tables III and IV with those using the analytical photon flux for pA in Table V. To normalize the photon cross sections, we divide the AA cross section by $2A$ because there is only a single photon source in pA and the proton target is a single nucleon. Due to the reduced minimum impact parameters, $\sigma(AA)/2A$ is (22 – 37)% lower for $c\bar{c}$ and (37 – 65)% lower for $b\bar{b}$ with $r_p = 0.6$ fm. The results differ least for small A where $R_A - r_p$ is reduced. Increasing r_p by 50% would decrease the $c\bar{c}$ cross sections (6 – 3.5)% and the $b\bar{b}$ cross sections by (11 – 7)%. Changing r_p has the largest effect for small A since R_A/r_p is smaller. The $b\bar{b}$ differences are largest because the energy is close to production threshold and high k corresponds to small impact parameter.

At the LHC, the maximum pA and AA energies differ, adding another variable to the comparison. Here, we compare $\sigma(AA)/2A$ directly with $\sigma(pA)$, using the analytic flux for both to maximize the parallelism. For equal pA and AA energies, the different b range is less significant at the LHC. The decrease in AA relative to pA is (18 – 23)% for $c\bar{c}$ and (24 – 30)% for $b\bar{b}$. As at RHIC, the effects are larger for heavier nuclei. Increasing r_p by 50% is only a (2 – 5)% effect with the bigger change for $b\bar{b}$.

The effect of the higher pA energy is significant. At the lower AA beam energy, the pA cross section is reduced (23 – 32)% for $c\bar{c}$ and (30 – 40)% for $b\bar{b}$ relative to the maximum pA energy. The major difference between the $c\bar{c}$ and $b\bar{b}$ results is likely due to the smaller x values probed in $c\bar{c}$ production. The increased energy has a larger effect on the cross section than the change in the minimum impact parameter. The energy dependence illustrates the desirability of obtaining energy excitation functions in both pA and AA interactions.

Tables VI and VII give the total monthly AA and pA $Q\bar{Q}$ production rates assuming a 10^6 s/month run. The $c\bar{c}$ rates are quite high. Of course, hadronization, branching ratios and detector acceptances will all reduce the observed rates. The $b\bar{b}$ rates are only significant at LHC. However, RHIC is a dedicated heavy ion facility, originally planned for more than 30 weeks of operation per year compared to 4 weeks of heavy ion running at the LHC and should thus accumulate more data than the tables indicate.

III. HADROPRODUCTION

Hadroproduction of heavy quarks in heavy ion collisions has been considered by many authors, see *e.g.* [38,39,49,50] and references therein. Here, we consider the special characteristics of heavy quark production in peripheral heavy ion collisions. Two aspects meriting our attention are the form of the parton densities at the nuclear surface and the overall appearance of the collision — could hadroproduction mimic a photon-nucleus or two-photon interaction? This section addresses the first issue while section VI considers the second.

At leading order, heavy quarks are produced via the reaction $N(P_1) + N(P_2) \rightarrow Q(p_1) + \bar{Q}(p_2) + X$. The LO parton reactions are $g(x_1P_1) + g(x_2P_2) \rightarrow Q(p_1) + \bar{Q}(p_2)$ and $q(x_1P_1) + \bar{q}(x_2P_2) \rightarrow Q(p_1) + \bar{Q}(p_2)$. The LO partonic cross sections are those of Eqs. (4) and (5) with \hat{s} , \hat{t}_1 , and \hat{u}_1 replaced by s , t_1 and u_1 . Thus the partonic couplings are a factor $\alpha_s(Q^2)/\alpha e_Q^2$ larger than direct photoproduction but have the same coupling strength as resolved photoproduction, as discussed in the previous section. The partonic invariants, s , t_1 , and u_1 , are now $s = (x_1P_1 + x_2P_2)^2$, $t_1 = (x_1P_1 - p_1)^2 - m_Q^2 = (x_2P_2 - p_2)^2 - m_Q^2$, and $u_1 = (x_2P_2 - p_1)^2 - m_Q^2 = (x_1P_1 - p_2)^2 - m_Q^2$.

The hadronic heavy quark production cross section is the convolution of two nuclear parton distributions with the partonic cross sections,

$$S^2 \frac{d^2\sigma_{AA \rightarrow Q\bar{Q}X}}{dT_1 dU_1 d^2b d^2r} = \int dz dz' \frac{dx_1}{x_1} \frac{dx_2}{x_2} \left(F_g^A(x_1, Q^2, \vec{r}, z) F_g^B(x_2, Q^2, |\vec{b} - \vec{r}|, z') s^2 \frac{d^2\sigma_{gg}}{dt_1 du_1} \right. \\ \left. + \sum_{q=u,d,s} \left\{ F_q^A(x_1, Q^2, \vec{r}, z) F_{\bar{q}}^B(x_2, Q^2, |\vec{b} - \vec{r}|, z') \right. \right.$$

$$+ F_q^A(x_1, Q^2, \vec{r}, z) F_q^B(x_2, Q^2, |\vec{b} - \vec{r}|, z') \left. \right\} s^2 \frac{d^2 \sigma_{q\bar{q}}}{dt_1 du_1} \Bigg) . \quad (12)$$

If the quark is detected, the hadronic invariants are again $S = (P_1 + P_2)^2$, $T_1 = (P_2 - p_1)^2 - m_Q^2$, and $U_1 = (P_1 - p_1)^2 - m_Q^2$ [37]. The partonic and hadronic invariants are now related by $s = x_1 x_2 S$, $t_1 = x_1 U_1$, and $u_1 = x_2 T_1$. Four-momentum conservation at leading order gives $x_{2\min} = -x_1 U_1 / (x_1 S + T_1)$. We again perform a fully leading order calculation using the MRST LO parton distributions and a one-loop evaluation of $\alpha_s(Q^2)$.

Since both the projectile and target partons come from nuclei, we consider the spatial dependence of the nuclear parton distributions, as suggested by shadowing measurements [55], in more detail. Shadowing in peripheral collisions could then be significantly different than in central collisions. We consider three scenarios: no shadowing, $S^i = 1$; homogeneous shadowing with the EKS98 parameterization, $S^i = \text{EKS98}$; and inhomogeneous shadowing, $S^i = \text{EKS98b}$, with spatial dependence included, as described in Refs. [38–42].

To obtain the AA cross sections, we integrate Eq. (12) over d^2r and d^2b . When $S^i = 1$ or EKS98, the only b dependence is in the nuclear density distributions and

$$\sigma_{AA} \propto \sigma_{NN} \int d^2b d^2r T_A(r) T_A(|\vec{b} - \vec{r}|) \quad (13)$$

where $T_A(r) = \int dz \rho_A(\vec{r}, z)$ is the nuclear profile function and σ_{NN} is the $Q\bar{Q}$ production cross section in an NN collision. When Eq. (12) is integrated over all b , $\sigma_{AA} \propto \sigma_{NN} A^2$ for $S^i = 1$. Homogeneous shadowing makes the A dependence nonlinear so that the integrated cross section is effectively $\sigma_{AA} \propto \sigma_{NN} A^{2\alpha}$ where α can be determined from the A dependence of the EKS98 parameterization. Of course when $S^i = \text{EKS98b}$, the full integral over b and r is needed in Eq. (12). In this section the impact parameter integral is restricted to $b > 2R_A$ to be consistent with the photoproduction results.

This calculation treats the nuclei as a continuous fluid, neglecting the lumpiness due to the individual nucleons. When $b > 2R_A$, only a handful of nucleon-nucleon collisions can occur, resulting in significant statistical fluctuations. These fluctuations, although unimportant for heavy quark production, may affect some of the observables used for impact parameter determination such as transverse energy or charged particle multiplicity.

The hadroproduction distributions for the heaviest ions are shown in Figs. 6-9. There are three curves for each colliding system. When the small x region is probed, the $S^i = 1$ result is the highest, EKS98 is the lowest, and EKS98b, with $b > 2R_A$, is between the other two. If we consider minimum impact parameters much larger than $2R_A$, the EKS98b curves would move even closer to the $S^i = 1$ results. The order is reversed for

$b\bar{b}$ production at RHIC because $x \sim M/\sqrt{S} \sim 0.05 - 0.1$ for $2m_b < M < 20$ GeV, in the gluon antishadowing region of the EKS98 parameterization. Thus the shadowed results lie above those with $S^i = 1$. The quark p_T and $Q\bar{Q}$ pair mass distributions are harder than the photoproduction results in Figs. 2-5 since now \sqrt{S} is the full nucleon-nucleon center of mass energy. In hadroproduction, the quark rapidity distribution is symmetric around $y_1 = 0$.

The $c\bar{c}$ AA cross sections and rates are given in Tables VIII and IX. The $b\bar{b}$ cross sections and rates are in Tables X and XI respectively. Shadowing has less effect on the total cross sections than in our previous calculations [38,39] which used earlier shadowing parameterizations [56,57] with stronger gluon shadowing at low x and weaker gluon antishadowing.

Shadowing effects depend on the final state rapidity and pair mass. The region away from $y_1 = 0$ tends to be most sensitive to the shadowing parameterization [41,42]. At RHIC, the effect grows with rapidity because at $y_1 \sim 0$ x is not small and shadowing is weak (charm) or x is in the antishadowing region (bottom). Higher positive rapidities correspond to lower x_2 for the target (stronger low x shadowing) and larger x_1 for the projectile (the EMC region), increasing the effect.

For $b\bar{b}$ production, the x region moves from antishadowing at $y_1 = 0$ to shadowing as y_1 increases. In Au+Au collisions at RHIC, $\sigma(S^i = \text{EKS98})/\sigma(S^i = 1) = 1.22$ at $y_1 = 0$ and 0.917 at $y_1 = 2.5$. At the LHC, the cross section varies less with rapidity because both the target and projectile momentum fractions are in the shadowing region. In fact shadowing tends to decrease slightly with rapidity because S^i increases more with x_1 than it decreases with x_2 .

Nuclear shadowing is more important at the LHC than at RHIC because the higher energy collisions probe smaller x values. Shadowing is also larger for $c\bar{c}$ than $b\bar{b}$ because the lighter charm quark is produced by lower x partons than b quarks. Homogeneous shadowing reduces the $c\bar{c}$ total cross section by (3 – 5)% at RHIC while at the LHC the reduction is (18 – 34)%. As expected, the reduction is largest for the heaviest nuclei. With the inhomogeneous shadowing parameterization, EKS98b, the $c\bar{c}$ cross section is reduced by (1 – 2)% at RHIC and $\sim 10\%$ at LHC. The $b\bar{b}$ cross section is antishadowed at RHIC by (6 – 20)% using EKS98, reduced to (3 – 8)% with EKS98b. At the LHC, the $b\bar{b}$ cross section is reduced by (10 – 19)% with EKS98 and $\sim 6\%$ with EKS98b. At large b , any inhomogeneity reduces the effect of shadowing. The larger the impact parameter cut, the closer the peripheral AA events mimic hadroproduction in free proton collisions.

A direct comparison with the photoproduction cross sections in Tables III and IV shows that the only rate comparable to hadroproduction at RHIC is $c\bar{c}$ photoproduction in Au+Au collisions when the same impact parameter range is considered. The photoproduction cross section is ~ 25 mb, comparable to the 33 mb hadroproduction cross section. With lead beams at the LHC, the $c\bar{c}$ photoproduction cross section is actually larger than the hadroproduction cross section. The $b\bar{b}$ photoproduction cross section is

always much lower than that of hadroproduction.

The hadroproduction cross sections tend to be larger than photoproduction cross sections for several reasons. In hadroproduction, the full \sqrt{S} is available for heavy quark production while coherent photon emission requires $\sqrt{S_{\gamma N}} \ll \sqrt{S}$. The lower energy reduces the cross section and restricts the x range of the gluons taking part in the interactions. Thus hadroproduction probes smaller x values than photoproduction. At low x the gluon densities are larger than the photon flux.

The minimum bias pA results with $S^i = 1$ and $S^i = \text{EKS98}$ are presented in Tables XII and XIII for charm and bottom respectively. We report the minimum bias pA cross sections only since it is difficult to select peripheral pA events. Shadowing is less important than in AA collisions since the pA cross section is linear in S^i while the AA cross section is quadratic in S^i . The minimum bias cross section is proportional to A for $S^i = 1$. A comparison of the RHIC minimum bias pA and the peripheral AA cross sections shows that the pA cross section without shadowing is equal to the AA cross section divided by $(1/A) \int d^2b T_{AA}(b > 2R_A)$, as expected. There is no corresponding factor of A for photoproduction so the hadroproduction pA cross sections are always bigger than the photoproduction cross sections in pA . Recent studies have shown that a comparison of hadroproduction in pA and pp collisions at the same energies can provide detailed information on nuclear shadowing effects [58]. In this case, there is no difference in flux between pA and AA collisions as there is in photoproduction. Such studies could provide important input to the AA collisions discussed here.

The variations in the cross section due to quark mass and QCD scale are similar in both hadroproduction and photoproduction. However, the additional NLO corrections are larger in hadroproduction. Even at NLO the calculations do not always agree with data. The measured B^+ production rate in $p\bar{p}$ collisions at $\sqrt{S} = 1800$ GeV is $2.9 \pm 0.2 \pm 0.4$ times the NLO calculation [59]. The reason for this discrepancy is unknown but some non-standard suggestions have been made [18,19]. The discrepancy may also be due to an incomplete understanding of the hadronization process [60].

The major uncertainty for hadroproduction in peripheral collisions is the minimum impact parameter. There is no known method for effectively selecting very large-impact parameter hadronic events or, alternatively, collisions with a small but well defined number of participants. Zero degree calorimeters (ZDCs) can be used to select events with a small number of spectator neutrons but these come from a poorly defined range of impact parameters. For this reason, peripheral AA collisions may best be studied by comparing different processes in a ZDC-selected data set. These different processes, such as heavy quark and gauge boson production [42], could be used to compare nuclear parton densities for several species at a variety x and Q^2 values.

IV. TWO-PHOTON PRODUCTION

Heavy quark pairs can also be produced in purely electromagnetic photon-photon collisions. This process has been studied at e^+e^- colliders. However, in ion colliders the cross sections are enhanced since the $\gamma\gamma$ luminosity increases as Z^4 .

The $\gamma\gamma$ luminosity has been calculated by many authors [61]. Naively, it is given by the convolution of the photon fluxes from two ultrarelativistic nuclei. The photon flux from one nucleus is the integral of $d^3N_\gamma/dk d^2r$ in Eq. (10) over r excluding the nuclear interior. Not all the flux is usable because, when the nuclei actually collide, the two-photon interaction products will be lost amongst the much denser hadronic debris. The usable flux is limited by the requirement that the nuclei do not interact hadronically. This is typically done by requiring that $b > 2R_A$. However, when the photon energy is close to the kinematic limit, $k_{\max} \approx \gamma_L \hbar c / R_A$, the flux is sensitive to the exact choice of R_A . To reduce the sensitivity to R_A , we calculate the probability, $P(b)$, of a hadronic interaction as a function of impact parameter,

$$P(b) = 1 - \exp \left[- \sigma_{NN}^{\text{tot}}(s) \int d^2r T_A(r) T_B(|\vec{b} - \vec{r}|) \right], \quad (14)$$

and use it to calculate the effective photon flux. Woods-Saxon density distributions [44] are used to calculate the nuclear overlap integral. The nucleon-nucleon total cross section, σ_{NN}^{tot} , is 52 mb at 200 GeV and 93 mb at 5.5 TeV [20]. We use the total cross section to exclude any interaction which could cause the nuclei to break up. This soft cutoff on the flux reduces the effective two-photon luminosity by a few percent for $k \ll \gamma_L \hbar c / R_A$, rising to about 15% at the kinematic limit compared to a hard cutoff with $R_A = 1.16(1 - 1.16A^{-2/3})A^{1/3}$ fm. We also exclude the flux when the heavy quarks are produced inside one of the nuclei. Although these heavy quarks would probably survive, the resulting interactions are likely to disrupt the nucleus, making the collision appear hadronic. With these exclusions, the differential $\gamma\gamma$ luminosity is

$$\frac{d\mathcal{L}_{\gamma\gamma}}{dk_1 dk_2} = \mathcal{L}_{AA} \int_{b>R_A} \int_{r>R_A} d^2b d^2r \frac{d^3N_\gamma}{dk_1 d^2b} \frac{d^3N_\gamma}{dk_2 d^2r} P(|\vec{b} - \vec{r}|). \quad (15)$$

The two-photon center of mass energy, $\sqrt{S_{\gamma\gamma}}$, is given by the photon energies, $S_{\gamma\gamma} = 4k_1 k_2$. This $S_{\gamma\gamma}$ is equivalent to W^2 , commonly used in other two-photon calculations. The maximum $\sqrt{S_{\gamma\gamma}}$ is $2k_{\max} = 2\gamma_L \hbar / R_A$, given in Table II. This limit is a factor of $(\hbar c / m_p R_A)^2$ smaller than \sqrt{S} , a factor of 10^{-3} for gold or lead. Indeed, $2k_{\max} < 2m_b$ for I+I and Au+Au collisions at RHIC. Thus heavy quark production in this channel should be much smaller than for photo- and hadroproduction.

As in photoproduction, there are also direct and resolved contributions. Either one or both of the photons [15] can resolve itself into partons. At the parton level, the single-

resolved photon case is equivalent to photoproduction while the double-resolved photon situation is equivalent to hadroproduction. Both of these contributions are included here. The diagrams for all of these processes are shown in Fig. 10.

The LO cross section for heavy quark production in direct two-photon interactions is also proportional to B_{QED} , as in Eq. (1) for direct photoproduction, but with different couplings,

$$s^2 \frac{d^2 \sigma_{\gamma\gamma}}{dt_1 du_1} = 6\pi\alpha^2 e_Q^4 B_{\text{QED}}(s, t_1, u_1) \delta(s + t_1 + u_1) , \quad (16)$$

where $s = (k_1 + k_2)^2 = S_{\gamma\gamma}$, $t_1 = (k_1 - p_1)^2 - m_Q^2$, and $u_1 = (k_2 - p_1)^2 - m_Q^2$. Here $t_1 = U_1$ and $u_1 = T_1$ for a detected quark. The $\gamma\gamma \rightarrow Q\bar{Q}$ cross section is a factor of $6e_Q^2\alpha/\alpha_s(Q^2)$ smaller than the partonic $\gamma g \rightarrow Q\bar{Q}$ cross section, Eq. (1). A factor of 3 comes from the three quark colors while another factor of 2 is from the spin averages. The ratio $\alpha/\alpha_s(Q^2)$ reduces the cross section for two-photon production relative to photoproduction. The same two Compton diagrams apply to both two-photon production and photoproduction except that a second photon replaces the gluon in $\gamma\gamma$ interactions.

The direct cross section is the convolution of the partonic two-photon cross section with the two-photon luminosity for photon energies k_1 and k_2 ,

$$S_{\gamma\gamma}^2 \frac{d^2 \sigma_{\gamma\gamma \rightarrow Q\bar{Q}}^{\text{dir}}}{dT_1 dU_1} = \int dk_1 dk_2 \frac{d\mathcal{L}_{\gamma\gamma}}{dk_1 dk_2} s^2 \frac{d^2 \sigma_{\gamma\gamma}}{dt_1 du_1} . \quad (17)$$

The photon fluxes are exponentially suppressed for $k \geq \gamma_L \hbar / R_A$.

The resolved processes follow from the discussion in Section II. The cross section for singly resolved production of heavy quarks is

$$S_{\gamma\gamma}^2 \frac{d^2 \sigma_{\gamma\gamma \rightarrow Q\bar{Q}}^{1\text{-res}}}{dT_1 dU_1} = 2 \int dk_1 dk'_2 \int \frac{dx_2}{x_2} \frac{d\mathcal{L}_{\gamma\gamma}}{dk_1 dk'_2} f_g^\gamma(x_2, Q^2) \hat{s}^2 \frac{d^2 \sigma_{\gamma g}}{d\hat{t}_1 d\hat{u}_1} , \quad (18)$$

where the partonic invariants, $\hat{s} = (k_1 + x_2 k_2)^2 = x_2 S_{\gamma\gamma}$, $\hat{t}_1 = (k_1 - p_1)^2 - m_Q^2$, and $\hat{u}_1 = (x_2 k_2 - p_1)^2 - m_Q^2$, are related to the total invariants by $\hat{t}_1 = U_1$ and $\hat{u}_1 = x_2 T_1$ and $k'_2 = x_2 k_2$. The partonic cross section, $\sigma_{\gamma g}$, is the photoproduction cross section in Eq. (1). The cross section for double-resolved heavy quark production is

$$S_{\gamma\gamma}^2 \frac{d^2 \sigma_{\gamma\gamma \rightarrow Q\bar{Q}}^{2\text{-res}}}{dT_1 dU_1} = \int dk'_1 dk'_2 \int \frac{dx_2}{x_2} \int \frac{dx_1}{x_1} \frac{d\mathcal{L}_{\gamma\gamma}}{dk'_1 dk'_2} \left[f_g^\gamma(x_1, Q^2) f_g^\gamma(x_2, Q^2) \hat{s}^2 \frac{d^2 \sigma_{gg}}{d\hat{t}_1 d\hat{u}_1} \right. \\ \left. + \sum_{i=u,d,s} (f_q^\gamma(x_1, Q^2) f_q^\gamma(x_2, Q^2) + f_q^\gamma(x_1, Q^2) f_q^\gamma(x_2, Q^2)) \hat{s}^2 \frac{d^2 \sigma_{q\bar{q}}}{d\hat{t}_1 d\hat{u}_1} \right] , \quad (19)$$

where $k'_2 = x_2 k_2$, $k'_1 = x_1 k_1$ and the partonic invariants, $\hat{s} = (x_1 k_1 + x_2 k_2)^2 = x_1 x_2 S_{\gamma\gamma}$, $\hat{t}_1 = (x_1 k_1 - p_1)^2 - m_Q^2$, and $\hat{u}_1 = (x_2 k_2 - p_1)^2 - m_Q^2$, are related to the total invariants by $\hat{t}_1 = x_1 U_1$ and $\hat{u}_1 = x_2 T_1$. The partonic cross sections, $\sigma_{q\bar{q}}$ and σ_{gg} , are given in Eqs. (4) and (5).

The full two-photon heavy quark cross section is the sum of all three contributions,

$$S_{\gamma\gamma}^2 \frac{d^2\sigma_{\gamma\gamma\rightarrow Q\bar{Q}}}{dT_1 dU_1} = S_{\gamma\gamma}^2 \frac{d^2\sigma_{\gamma\gamma\rightarrow Q\bar{Q}}^{\text{dir}}}{dT_1 dU_1} + S_{\gamma\gamma}^2 \frac{d^2\sigma_{\gamma\gamma\rightarrow Q\bar{Q}}^{1\text{-res}}}{dT_1 dU_1} + S_{\gamma\gamma}^2 \frac{d^2\sigma_{\gamma\gamma\rightarrow Q\bar{Q}}^{2\text{-res}}}{dT_1 dU_1}. \quad (20)$$

In Eqs. (18) and (19) the scale entering into the photon parton densities and $\alpha_s(Q^2)$ has been set equal to $4m_Q^2$ due to the structure of the $\gamma\gamma$ luminosity. Changing the scale from $4m_T^2$ to $4m_Q^2$ increases the single-resolved cross section by about 10%, while the double-resolved cross section changes by at most 2%.

Figures 11-14 show the corresponding $c\bar{c}$ and $b\bar{b}$ production distributions. The RHIC results are shown for Si+Si collisions since that is the largest A for which $2k_{\text{max}} > 2m_b$. The Pb+Pb results are shown for LHC. The integrated cross sections for all the other nuclei are given in Tables XIV and XV. The quark p_T and rapidity and the $Q\bar{Q}$ pair invariant mass distributions are narrower for the heavier nuclei due to the lower associated $\sqrt{S_{\gamma\gamma}}$. The production is mostly direct. The single and double resolved p_T and mass distributions are narrower than the direct results at all energies.

The rapidity distributions are symmetric around $y_1 = 0$ except for the singly resolved processes. Since either photon may be resolved, we give the single-resolved rapidity distributions in both cases. The total single-resolved rapidity distribution is the sum. We present both to be consistent with the direct and double-resolved calculations. The factor of two in the cross section, Eq. (18), is included in the single-resolved transverse momentum and invariant mass distributions.

Direct $\gamma\gamma$ production dominates two-photon production of heavy quarks. For $c\bar{c}$ pairs, at RHIC the single-resolved cross section is (0.6 – 1.6)% of the direct production. Double-resolved production is (2.5 – 3.3)% of the single resolved. The single-resolved to direct ratio increases with A or, equivalently, decreasing $\sqrt{S_{\gamma\gamma}}$. Interestingly, the single-to double-resolved cross section ratios decrease with increasing A , presumably due to the larger $q\bar{q}$ component at lower energies, closer to production threshold where the quark distribution in the photon is dominant. At LHC, the single-resolved cross section is 4.5% of the direct production. The single-resolved component is higher at LHC because of the higher energy. However, double-resolved production is only 2.1% of the single resolved because the higher beam energy reduces x , increasing the photon gluon distribution but the gg contribution is too small to make up the difference. The situation changes for $b\bar{b}$ production. At RHIC, single-resolved production is (0.3 – 0.7)% of the direct component but double-resolved production is 20% of the single resolved. The lower energy strongly reduces the single-resolved cross section relative to the direct $\gamma\gamma$ but has less effect

on double-resolved production because of the strong $q\bar{q}$ component. At the LHC the single-resolved result is 10% of the direct while the double-resolved is reduced relative the single-resolved by the same factor. The LEP results suggest relatively low quark masses and a large resolved cross section [62]. Our resolved contributions are smaller, possibly because the $\gamma\gamma$ luminosity at LEP drops more slowly with $\sqrt{S_{\gamma\gamma}}$ than do the $\gamma\gamma$ luminosities for ions.

These results are for all $Q\bar{Q}$ pairs, as are the results shown for the other channels. However, a significant fraction of the pairs have masses below the $H\bar{H}$ threshold, especially at RHIC. Pairs with mass $M < 2m_H$ are also produced in photo- and hadroproduction. A few of these pairs will become quarkonium states [63]. Most of them will hadronize into heavy-flavor hadrons, thanks to the presence of accompanying particles. A soft gluon can provide the energy to bring the quarks on shell. However, two-photon interactions occur in a vacuum with no available energy source. Pairs with $M < 2m_H$ may annihilate if they do not form quarkonium. Tables XIV and XV compare the total cross sections for all $Q\bar{Q}$ pairs to those pairs with $M > 2m_H$. In both cases, the two-photon cross sections are several orders of magnitude below those for hadroproduction and photoproduction. The $c\bar{c}$ cross sections are $\mathcal{O}(\text{nb})$ rather than mb and the $b\bar{b}$ cross sections are $\mathcal{O}(\text{pb})$ rather than μb .

The requirement $M > 2m_H$ dramatically reduces charm production. At RHIC the $c\bar{c}$ cross section is reduced a factor of 3–6 for direct $\gamma\gamma$, 4–16 for single resolved, and 5–22 for the double-resolved. The higher LHC energy lessens the threshold effect considerably; the reduction is only a factor of ~ 1.9 for direct and single-resolved production and ~ 2.5 for double-resolved production. These reductions depend strongly on the heavy quark mass. Our m_c , 1.2 GeV, is about $0.64m_D$ but the reduction is much smaller for larger charm masses. This threshold effect reduces the overall sensitivity of the calculation to the charm quark mass. Charm production calculations with a threshold cut match recent LEP data [64], indicating that the reduced cross sections are more appropriate experimentally.

The threshold reduction is smaller for bottom quarks since $m_b = 4.75 \text{ GeV} \approx 0.9m_B$. At RHIC, the cross section is a factor of ~ 1.5 smaller for direct photoproduction and 1.5 – 2.5 for single- and double-resolved production. At the LHC, all the cross sections are reduced by (10 – 20)%. The threshold effect is more important for larger A because $\sqrt{S_{\gamma\gamma}}$ falls with increasing R_A .

Figures 15 and 16 show the ratios for $Q\bar{Q}$ production with and without the threshold cut as a function of p_T and rapidity for $c\bar{c}$ production at RHIC and $b\bar{b}$ production at the LHC. An invariant mass cut simply selects pairs with $M > 2m_H$. The threshold cut only affects low p_T quarks. The minimum p_T for a quark to pass the $2m_H$ threshold is $p_T \geq \sqrt{m_H^2 - m_Q^2}$, 1.4 GeV for $m_c = 1.2 \text{ GeV}$ and 2.3 GeV for $m_b = 4.75 \text{ GeV}$. Naturally, with a larger quark mass, the minimum p_T would decrease. The larger threshold effect for charm production appears because the peak of the p_T distributions in Figs. 11 and 13

is below this minimum p_T . The average p_T for bottom production is larger so that more of the cross section survives the threshold cut. On the other hand, the cross section is reduced most near $y_1 = 0$ where low p_T dominates the rapidity distribution. At large rapidities, the pair $Q\bar{Q}$ mass is always above threshold. The threshold has the smallest effect on direct production and the strongest on the double-resolved cross sections, as can be expected due to the decreasing effective energy available for each process.

Energy conservation requires that a heavy quark pair produced with mass M retain that energy. To compensate for the ‘mass deficit’, $M - 2m_H$, the final state mesons must have less kinetic energy than the initial state quarks. Near threshold, the quark p_T and rapidity distributions presented in Figs. 11-14 will differ from the final state meson distributions.

We do not present any two-photon results for pA since the cross sections are very small and the proton substructure could play a role [65]. On the other hand, the small proton radius allows pA collisions to reach higher $\gamma\gamma$ energies than the corresponding AA collisions so that $b\bar{b}$ production would be energetically accessible in pI and pAu collisions at RHIC.

The major uncertainties in the $\gamma\gamma$ calculations are the quark masses and the $\gamma\gamma$ luminosity. In contrast to hadroproduction and photoproduction, the higher order corrections seem fairly well known. If the $\gamma\gamma$ luminosity can be sufficiently well determined, heavy quark production could then be used to fix the quark masses. The uncertainties in the $\gamma\gamma$ luminosity are comparable to those for γA and also depend on the minimum impact parameter. However, final states with known $\gamma\gamma$ couplings can be used for calibrations. Lepton pair production covers the full range of $S_{\gamma\gamma}$ and may be accurately calculated using only electrodynamics. Production of well known mesons may also help check the luminosity. With these calibrations, $\sigma(\gamma\gamma \rightarrow Q\bar{Q})$ could clearly be measured to the 10% level. At that point, other theoretical uncertainties will dominate and the measurements can be used to determine the heavy quark masses. These masses can then be used in calculations of other processes.

V. THEORETICAL COMPARISONS

In this section, we compare and contrast some of the calculational uncertainties in our results. We have performed fully LO calculations, including LO parton densities and a one-loop evaluation of $\alpha_s(Q^2)$. We first compare our LO results with NLO calculations. We also describe the dependence of our results on the chosen quark mass and scale.

At any order, the partonic cross sections for all three processes studied may be expressed in terms of dimensionless scaling functions $f_{ij}^{(k,l)}$ that depend only on the variable $\eta = \hat{s}/4m^2 - 1$ [66],

$$\hat{\sigma}_{ij}(\hat{s}, m_Q^2, Q^2) = \frac{(\alpha e_Q^2)^q \alpha_s^p(Q^2)}{m_Q^2} \sum_{k=0}^{\infty} (4\pi\alpha_s(Q^2))^k \sum_{l=0}^k f_{ij}^{(k,l)}(\eta) \ln^l \left(\frac{Q^2}{m_Q^2} \right), \quad (21)$$

where \hat{s} is the square of the partonic center of mass energy, m_Q is the heavy quark mass, and Q^2 is the scale. The cross sections are expanded in powers of $\alpha_s(Q^2)$ and α . The exponents q and p depend on the initial process: $q = 1, p = 1$ direct photoproduction; $q = 0, p = 2$ hadroproduction; and $q = 2, p = 0$ direct two-photon production. The summation over k includes all corrections beyond LO which only involve powers of $\alpha_s(Q^2)$ with $k = 0$ corresponding to the Born and $k = 1$ to the NLO cross sections. It is only at NLO that the logarithms $\ln^l(Q^2/m_Q^2)$ appear. Two scales, for renormalization and factorization, appear in the calculation but they are generally assumed to be the same since this choice is used in fits of the parton densities. The total cross sections are obtained by convoluting the partonic cross sections with the parton distribution functions or photon fluxes. The scale Q^2 enters the total cross section in the evaluation of $\alpha_s(Q^2)$ and in the parton densities of the proton or photon (for resolved processes).

For a fully consistent calculation of the partonic cross sections, $\alpha_s(Q^2)$ should be evaluated to one loop when $k = 0$, two loops when $k = 1 \dots$. The strong coupling constant has been evaluated up to three loops, corresponding to $k = 2$. However, a consistent evaluation of the cross section, order-by-order in partonic cross section, parton distribution, and $\alpha_s(Q^2)$, is usually not done. One is usually interested only in the effect of the next-higher-order corrections to the total cross section and it is only possible to measure the change by leaving other inputs, such as the parton densities, the same at all orders. Thus, theoretical ratios of the total NLO to LO cross sections, the K factors, are typically independent of the observable [67,68].

The hadroproduction K factor is larger for ‘light’ heavy quarks, low p_T , and low M . As the heavy quark mass increases, K drops from 2.5 – 3 for $c\bar{c}$ to 1.8 – 2.3 for $b\bar{b}$ in this energy range. For direct photoproduction, the K factors are smaller. The calculated K factors for direct photoproduction of bottom are 1.4 – 1.7 for $\sqrt{S_{\gamma p}} = 314$ and 1265 GeV respectively [29]. The LO resolved photoproduction results, $\mathcal{O}(\alpha_s^2)$ with $p = 2, q = 0$ in Eq. (21) as at LO in hadroproduction, are typically used without NLO corrections in photoproduction so that the same order in $\alpha_s(Q^2)$ is used for both direct and resolved photoproduction. Thus the K factor would only be constant with rapidity and transverse momentum for direct photoproduction, not for the sum in Eq. (8). However, the resolved contribution is always rather small and should not significantly change the K factor. The NLO $\gamma\gamma$ corrections are smaller still, $K = 1.33$ for $c\bar{c}$ and 1.24 for $b\bar{b}$ in direct $\gamma\gamma$, dropping to $K \sim 1.15$ for $c\bar{c}$ and 1.21 for $b\bar{b}$ single-resolved production [15]. The small K factor for direct $\gamma\gamma$ should perhaps not be a surprise since, in a sense, $\gamma\gamma$ is the cleanest determination of the K factor because there is no parton density, $\alpha_s(Q^2)$ or scale dependence at LO.

This K factor, calculated with both the LO and NLO scaling functions convoluted with NLO parton densities and two-loop evaluations of $\alpha_s(Q^2)$, does not mesh with a full

LO calculation using LO parton densities. The incompatibilities include the difference in $\alpha_s(Q^2)$ evaluated at one and two loops. In the MRST LO densities, $\Lambda_3 = 0.204$ GeV so that $\alpha_s^{1\text{-loop}} = 0.287$ and $\alpha_s^{2\text{-loops}} = 0.220$. The hadronic LO cross sections calculated with the MRST HO distributions [43] are $\sigma_{\text{LO}} = 196 \mu\text{b}$ at 200 GeV, rising to 6.03 mb at 5.5 TeV, compared with $\sigma_{\text{NLO}} = 382 \mu\text{b}$ at 200 GeV and 5.83 mb at 5.5 TeV. The NLO evaluation is two times larger at RHIC, but at the LHC, the results agree within 3%. The difference is mostly due to the higher one-loop $\alpha_s(Q^2)$. Because of these variations, we do not apply any K factors to our LO calculations.

Our calculations for all three processes use the same values of m_Q and Q^2 . The values are chosen to agree with hadroproduction data at fixed target energies. Photoproduction and two-photon data imply larger charm quark masses than used here. The typical charm mass used for those processes, 1.6 – 1.7 GeV, predict lower cross sections than those employing the quark masses obtained from hadroproduction. One can speculate as to why this is true. It may be that the incident quarks and gluons in hadroproduction interact with the virtual heavy quark at its current quark mass while the almost real photons interact with the constituent c and b quarks. The constituent quark mass is larger than the current quark mass and is thus more compatible with the photoproduction data. On the other hand, since $K > 2$ for hadroproduction, unincorporated higher order corrections may explain the apparent need for different quark masses. Near threshold, the $b\bar{b}$ cross section has been evaluated to next-to-next-to-leading order and next-to-next-to-leading logarithm (NNLO-NNLL). Recent results from HERA-B [69] agree very well with the predicted $30 \pm 8 \pm 10$ nb NNLO-NNLL cross section [66] calculated with $m_b = 4.75$ GeV. The NLO evaluation at the same energy is a factor of two smaller, suggesting that NLO calculations require smaller bottom quark masses. However, the NNLO-NNLL expansion is invalid far away from threshold so that the importance of further higher order corrections is difficult to quantify.

Figure 17 shows the quark mass dependence of the total cross sections for all three processes. We plot $\sigma(m_Q)/\sigma(m_0)$ where $m_0 = 1.2$ GeV for charm and 4.75 GeV for bottom. The scale used is $Q^2 \propto 4m_c^2$ and m_b^2 for charm and bottom, respectively. Results are shown for $\sqrt{S} = 250$ GeV Si+Si collisions at RHIC and 5.5 TeV Pb+Pb collisions at the LHC. The mass sensitivity is smaller at higher energies, as expected. For a given energy, hadroproduction is the least mass dependent. The direct photoproduction and two-photon production processes have nearly the same mass dependence. Resolved production has a stronger mass dependence, especially at RHIC. The mass dependence is stronger for charm than bottom, mainly because the charm mass is varied by 50%, from 1.2 to 1.8 GeV while the bottom mass is only varied 18%, from 4.25 to 5.00 GeV.

The photoproduction and two-photon cross sections are more mass dependent than hadroproduction at the same energies. The maximum γp collision energies, $\sqrt{S_{\text{max}}}$, are a factor of 4 – 6 less than \sqrt{S} in AA collisions at both colliders. The maximum photon energy fraction, $\hbar c/m_p R_A$, is ~ 0.03 for gold or lead, rising to 0.1 for silicon, much smaller than the maximum parton energy fraction, $x = 1$. This energy deficit is difficult to overcome and is only compensated for by the photon flux factor of Z^2

in charm production with the heaviest ions. The energy difference is more important for bottom production, especially at RHIC since $\sqrt{S_{\text{max}}}$ is close to the $b\bar{b}$ threshold. As Table I shows, lighter ions may be advantageous for photoproduction studies since the higher photon energies and accelerator luminosities can compensate for the smaller cross sections. The energy deficit in $\gamma\gamma$ production is even larger, 9.8 – 31.25 between the maximum $\sqrt{S_{\gamma\gamma}}$ and \sqrt{S} . For the heaviest ions at RHIC, the maximum $\sqrt{S_{\gamma\gamma}}$ is below the $b\bar{b}$ threshold. In these collisions, even charm is not far from threshold. The factor of Z^4 cannot compensate for such an energy deficit. The 1 mb $c\bar{c}$ cross section for $M > 2m_c$ at LHC is still a factor of 1000 lower than those of the other processes. Thus good experimental separation is essential for observing clean $\gamma\gamma$ interactions.

The photo- and hadroproduction scale dependence is small. The cross sections only change a few percent between $Q^2 = m_Q^2$ and $4m_Q^2$ because increasing the scale decreases $\alpha_s(Q^2)$ but increases the gluon density $F_g^p(x, Q^2)$ and vice versa. The two effects largely cancel. At NLO, the scale dependence is usually larger for charm and bottom quarks than at LO [12] because $\alpha_s(Q^2)$ multiplies the logarithm $\ln(Q^2/m_Q^2)$. The scale dependence only enters through the resolved contributions in $\gamma\gamma$ production where the effect is a factor of 1.5 – 2 on single-resolved production and 1.05 – 1.4 on double-resolved production. However, the total cross section is essentially unaffected because the direct contribution is independent of scale.

VI. EXPERIMENTAL SEPARATION

To study ultra-peripheral heavy quark production, it is necessary to be able to disentangle the three channels. Photoproduction, hadroproduction, and two-photon interactions may be separated on the basis of overall event characteristics. The signatures that can be used to distinguish between production processes are whether there are rapidity gaps in the event and whether the nuclei break up. Nuclear breakup can be measured with downstream ZDCs.

Other variables may be helpful in separating event classes. The event multiplicity is lower for photoproduction and two-photon interactions because less energy is available. The multiplicity also depends on the details of the interaction. For two-photon interactions, the total event p_T should be less than $2\hbar c/R_A$. Unfortunately, it is necessary to reconstruct the entire event to measure the total p_T . This is difficult in $Q\bar{Q}$ events. Because of these difficulties, multiplicity and p_T will not be further considered here as a separation factor.

This section will focus on isolating clean photoproduction and two-photon final states. The large hadroproduction cross sections are a background to these events. The cuts discussed here are geared toward reducing the hadroproduction background and thereby differentiating between the three production processes. RHIC data [2] show that almost

all hadronic interactions break up both nuclei. In contrast, photoproduction should only dissociate the target nucleus while two-photon interactions should leave both nuclei intact. However, the photoproduction and two-photon interactions occur at moderate impact parameters, less than 50 (500) fm at RHIC (LHC), where one or more additional photons may be exchanged.

For heavy nuclei like lead or gold, the additional photons can excite one or both nuclei, leading to nuclear breakup. Except for the common impact parameter, these additional photons are independent of the two-photon or photonuclear events [70]. The probabilities for excitation are significant. The probability of a single given nucleus being excited in a collision at $b = 2R_A$ is about 30% with gold at RHIC, rising to 35% for lead at the LHC [1]. As b rises, the excitation probability drops as $1/b^2$. The breakup probability scales as $A^{10/3}$ so that for even slightly lighter nuclei like argon or silicon the breakup probability is considerably reduced. Since the nuclear breakup probabilities are independent of each other, the probability for both nuclei to dissociate is simply the square of the single dissociation probability.

One way to select photoproduction events is to eliminate events where both nuclei break up. This should eliminate almost all of the hadroproduction events while retaining most of the photoproduction and two-photon interactions. Unfortunately, there are no calculations of the hadronic interaction cross sections without accompanying nuclear breakup. Indeed, such a calculation is problematic because too little is known about the recoil energy transfer in the nucleus. However, using a Glauber calculation, we find that the cross section for a single nucleon-single nucleon interaction in an Au+Au collision is about 700 mb, 10% of the total hadronic cross section. At RHIC and LHC energies even soft nuclear interactions involve significant energy transfer. Thus phase space considerations dictate that the interacting nucleons are likely to be ejected from the nucleus. There could then be considerable momentum transferred to the nuclear fragments. Here we assume that each nucleus has a 10% chance of remaining intact. With these assumptions, the heavy quark hadroproduction cross sections with one nucleus remaining intact are not too different from those presented in Section III. The 10% chance of remaining intact may be high, but, to be conservative, we will use the rates in Section III to calculate the hadronic backgrounds to photoproduction.

The rejection factor R is the probability of finding a rapidity gap with width y in a hadronic collision, $R \sim \exp(-ydN/dy)$, where dN/dy is the average multiplicity per unit rapidity. Here, we will only consider charged particles but with a calorimeter to detect neutrals, the rejection would be enhanced. The UA1 collaboration parameterized the charged particle multiplicity as $dN_{\text{ch}}/dy \approx -0.32 + \ln \sqrt{S/\text{GeV}}$ [71]. Neglecting the small difference between $p\bar{p}$ and pp collisions, at midrapidity at RHIC, $dN_{\text{ch}}/dy \approx 2.6$ [72], rising to $dN_{\text{ch}}/dy \approx 4.4$ at the LHC. Most modern experiments use forward detectors like beam-beam counters to measure particle production over a wide rapidity range. These counters can be used to find rapidity gaps. Here we will consider two charged particle detectors each covering 2 units of rapidity on each side of a central detector,

representative of modern experiments. We scale the midrapidity multiplicities by 0.6 because dN_{ch}/dy decreases away from midrapidity.

For photoproduction, requiring a single rapidity gap will reject all but $R = \exp(-2 \times 0.6 \times 2.6) = 0.04$ of the hadronic interactions at RHIC while at LHC the rejection for a similar detector is $R = \exp(-2 \times 0.6 \times 4.4) = 0.005$. These factors, calculated for pp collisions, should be conservative for pA and AA collisions where there is typically more than a single nucleon-single nucleon collision. These factors would also apply to the rejection of photoproduction backgrounds when considering two-photon reactions. Since there are two rapidity gaps in two-photon interactions, these rejection factors are squared.

The CDF collaboration has experimentally observed comparable rejection factors in a study of diffractive bottom production [17]. They isolated a diffractively produced bottom sample from $p\bar{p}$ collisions [17] with a signal to noise ratio of 3:1 despite the fact that diffractive production was 1/160 of the total hadronic b cross section. This corresponded to $R = 0.002$, smaller than the R values calculated above. This is probably because the CDF forward counters cover 2.7 units of rapidity and are supplemented with forward calorimeters that detect neutrals. Thus the rejection factors are not unrealistic and could even be improved on with more solid angle coverage. Of course, for nuclear beams the higher multiplicities per participant pair should increase the rejection factors, even for single nucleon-single nucleon interactions, due to possible secondary interactions.

The rapidity gap requirements should reject relatively few signal events since photoproduction always leads to a rapidity gap. The exceptions are the events that are accompanied by additional electromagnetic interactions. A small fraction of these breakups will involve high energy photons which produce final state particles that fill in the rapidity gap, causing the signal event to be lost. Even at the LHC, the breakup probability due to high energy photons is quite small and events with additional particles should not appreciably affect the signal. If it is necessary to also require that one nucleus remains intact, then signal loss will need to be considered but such loss will not affect the viability of the measurement.

Other backgrounds are neglected here. Examples include single diffractive (hadronic) charm production and double-Pomeron interactions. Single diffractive production will have one rapidity gap and could potentially mimic charm photoproduction. However, the diffractive final state would be produced quite near the beam rapidity, forward of the predominantly photoproduced charm. Double-Pomeron charm production will be in the central region with two rapidity gaps. Because the Pomeron has such a short range, both single and double diffractive interactions can only occur over a very narrow range of impact parameters so that their AA cross sections should be small [73]. The other major background, beam-gas interactions, is detector and vacuum system specific and will not be discussed here.

Conservatively, both the rapidity gaps and nuclear breakup criteria should reject

more than 99% of the hadronic events. Although these criteria are not completely independent, comparing the numbers in Sections II - IV shows that application of either criteria should lead to a good signal to noise ratio for selecting either photoproduction or two-photon interactions. If 99% of the hadronic events with $b > 2R_A$ can be rejected, then hadroproduction is only a small background to photoproduction of heavy quarks, one that can be controlled to the degree necessary to measure shadowing by comparing pA and AA .

One could also select events with two rapidity gaps and no nuclear breakup to search for two-photon interactions. However, in almost all cases, the two-photon cross sections are a factor of at least 1,000 smaller than the photoproduction cross sections. This factor is smaller than the single-gap R calculated above as well as larger than rejection obtained by CDF and unlikely to be achieved in a real experiment. Selecting two-photon events may require completely reconstructing the events and using the low total p_T of the event as a final selection criteria. This reconstruction will necessarily have a very low overall efficiency, thus requiring very large data sets.

In conclusion, both rapidity gaps and the absence of nuclear breakup are effective criteria to separate photoproduction interactions. Charged-particle multiplicity and other event characteristics may also be useful in refining the event selection. Once a sample of photoproduction events have been isolated, charm and bottom production may be studied with conventional selection techniques such as prompt leptons, separated vertices, and D or B meson reconstruction.

VII. CONCLUSIONS

We have calculated the total cross sections, quark p_T and y distributions, and pair mass spectra for hadronic, photonuclear and two-photon production of heavy quark pairs using a consistent set of quark masses and scales. The hadronic processes have the largest cross sections, followed by photoproduction and two-photon interactions. However, using the characteristics of rapidity gaps and nuclear breakup, photoproduction and two-photon processes should be cleanly separable.

Photoproduction and two-photon measurements can be used to test the QCD calculations. Shadowing has a 10% effect on $c\bar{c}$ production with heavy nuclei at RHIC, rising to 20% at the LHC. By comparing the production cross sections in pA and AA collisions, most theoretical uncertainties cancel so that shadowing can be accurately measured if the photon flux is well known. By using appropriate calibration signals, it appears that the photon flux uncertainties can be understood and useful gluon shadowing measurements made.

R.V. thanks the Gesellschaft für Schwerionenforschung, the Niels Bohr Institute, and

the Grand Accélérateur National d'Ions Lourds for hospitality while this work was in progress. This work was supported in part by the Division of Nuclear Physics of the Office of High Energy and Nuclear Physics of the U.S. Department of Energy under Contract No. DE-AC-03-76SF00098 and by the Swedish Research Council (VR).

REFERENCES

- [1] G. Baur, K. Hencken and D. Trautmann, *J. Phys. G* **24**, 1457 (1998); G. Baur, K. Hencken, D. Trautmann, S. Sadovsky and Y. Kharlov, *Phys. Rep.* **364**, 359 (2002).
- [2] M. Chiu *et al.*, *Phys. Rev. Lett.* **89**, 012302 (2002).
- [3] S.R. Klein and J. Nystrand, *Phys. Rev. C* **60**, 014903 (1999).
- [4] C. Adler *et al.* (STAR Collaboration), nucl-ex/0206004, submitted to *Phys. Rev. Lett*; S. Klein (STAR Collab.), in proceedings of the 17th *Winter Workshop on Nuclear Dynamics*, Park City, UT, USA, 2001, nucl-ex/0104016.
- [5] S. Klein (STAR Collab.), in proceedings of *INPC 2001*, Berkeley, CA, USA, 2001, nucl-ex/0100018.
- [6] E. Lippmaa *et al.*, *FELIX: A full acceptance detector at the LHC*, CERN/LHCC 97-45, August, 1997.
- [7] K. Piotrkowski, *Phys. Rev. D* **63**, 071502 (2001).
- [8] N. Baron and G. Baur, *Phys. Rev. C* **48**, 1999 (1993).
- [9] M. Greiner, M. Vidović, C. Hofmann, A. Schäfer and G. Soff, *Phys. Rev. C* **51**, 911 (1995).
- [10] S.R. Klein, J. Nystrand and R. Vogt, *Eur. Phys. J. C* **21**, 563 (2001).
- [11] M. Vidović, M. Greiner and G. Soff, *J. Phys. G* **21**, 545 (1995).
- [12] P.L. McGaughey *et al.*, *Int. J. Mod. Phys. A* **10**, 2999 (1995).
- [13] S. Frixione, P. Nason and G. Ridolfi, *Nucl. Phys. B* **454**, 3 (1995).
- [14] A.V. Berezhnoy, V.V. Kiselev and A.K. Likhoded, *Phys. Rev. D* **62**, 074013 (2000).
- [15] M. Drees, M. Kramer, J. Zunft and P.M. Zerwas, *Phys. Lett. B* **306**, 371 (1993).
- [16] M. Acciarri *et al.* (L3 Collab.), *Phys. Lett. B* **453**, 83 (1999).
- [17] T. Affolder *et al.* (CDF Collab.), *Phys. Rev. Lett.* **84**, 232 (2000).
- [18] E.L. Berger, B.W. Harris, D.E. Kaplan, Z. Sullivan, T.M.P. Tait and C.E.M. Wagner, *Phys. Rev. Lett.* **86**, 4231 (2001).
- [19] A.P. Lipatov, V.A. Saleev and N.P. Zotov, hep-ph/0112114.
- [20] D.E. Groom *et al.* (Particle Data Group), *Eur. Phys. J. C* **15**, 1 (2000).
- [21] RHIC Conceptual Design Report (BNL-52195) 1989.
- [22] D. Brandt, LHC Project Report 450, December, 2000.
- [23] D. Brandt, in Proc. of the 6th CMS Heavy Ion Workshop, MIT, February 2002.
- [24] V.P. Goncalves and C.A. Bertulani, *Phys. Rev. C* **65**, 054905 (2002).
- [25] E. Witten, *Nucl. Phys. B* **120**, 189 (1977).
- [26] T. Sjöstrand, J.K. Storrow, and A. Vogt, *J. Phys. G* **22**, 893 (1996).
- [27] L.M. Jones and H.W. Wyld, *Phys. Rev. D* **17**, 759 (1978).
- [28] S.R. Klein and J. Nystrand, *Phys. Rev. Lett.* **84**, 2330 (2000).
- [29] J. Smith and W.L. van Neerven, *Nucl. Phys. B* **374**, 36 (1992).
- [30] M. Glück, E. Reya, and A. Vogt, *Phys. Rev. D* **46**, 1973 (1992); *Phys. Rev. D* **45**, 3986 (1992).
- [31] M. Drees and K. Grassie, *Z. Phys. C* **28**, 451 (1985).
- [32] H. Abramowicz, K. Charchula, and A. Levy, *Phys. Lett. B* **269**, 458 (1991).
- [33] K. Hagiwara, M. Tanaka, I. Watanabe, and T. Izubuchi, *Phys. Rev. D* **51**, 3197 (1995).

- [34] G.A. Schuler and T. Sjöstrand, Z. Phys. C **68**, 607 (1995); Phys. Lett. B **276**, 193 (1996).
- [35] H. Plochow-Besch, ‘PDFLIB: Proton, Pion and Photon Parton Density Functions, Parton Density Functions of the Nucleus, and α_s Calculations’, User’s Manual - Version 8.04, W5051 PDFLIB, 2000.04.17, CERN-ETT/TT.
- [36] W. Bartel *et al.* (JADE Collab.), Z. Phys. C **24**, 231 (1984).
- [37] G. Sterman *et al.* (CTEQ Collab.), Rev. Mod. Phys. **67**, 157 (1995).
- [38] V. Emel’yanov, A. Khodinov, S.R. Klein and R. Vogt, Phys. Rev. C **56**, 2726 (1997).
- [39] V. Emel’yanov, A. Khodinov, S.R. Klein and R. Vogt, Phys. Rev. Lett **81**, 1801 (1998).
- [40] V. Emel’yanov, A. Khodinov, S.R. Klein, and R. Vogt, Phys. Rev. C **59**, 1860 (1999).
- [41] V. Emel’yanov, A. Khodinov, S.R. Klein and R. Vogt, Phys. Rev. C **61**, 044904 (2000).
- [42] R. Vogt, Phys. Rev. C **64**, 044901 (2001).
- [43] A.D. Martin, R.G. Roberts, W.J. Stirling and R.S. Thorne, Eur. Phys. J. C **4**, 463 (1998); Phys. Lett. B **443** 301 (1998).
- [44] C.W. deJager, H. deVries and C. deVries, Atomic Data and Nuclear Data Tables **14**, 485 (1974).
- [45] K.J. Eskola, V.J. Kolhinen and P.V. Ruuskanen, Nucl. Phys. B **535**, 351 (1998); K.J. Eskola, V.J. Kolhinen and P.V. Ruuskanen, Eur. Phys. J. C **9**, 61 (1999).
- [46] H. Fritzsche and K.H. Streng, Phys. Lett. B **72**, 385 (1978).
- [47] Ch. Hofmann, G. Soff, A. Schäfer and W. Greiner, Phys. Lett. B **262**, 210 (1991).
- [48] F. Gelis and A. Peshier, Nucl. Phys. A **697**, 879 (2002).
- [49] R. Vogt, B.V. Jacak, P.L. McGaughey, and P.V. Ruuskanen, Phys. Rev. D **49**, 3345 (1994).
- [50] S. Gavin, P.L. McGaughey, P.V. Ruuskanen, and R. Vogt, Phys. Rev. C **54**, 2606 (1996).
- [51] J.C. Anjos *et al.* (E691 Collab.), Phys. Rev. Lett. **65**, 2503 (1990).
- [52] S. Frixione, in Proc. of *EPS01*, Budapest, Hungary, 2001, hep-ph/0111368.
- [53] J. Breitweg *et al.* (ZEUS Collab.), Eur. Phys. J C **2**, 247 (1998).
- [54] A. Trzcinska *et al.*, Phys. Rev. Lett. **87**, 082501 (2001).
- [55] T. Kitagaki *et al.* (Fermilab E745 Collab.), Phys. Lett. B **214**, 281 (1988).
- [56] K.J. Eskola, J. Qiu and J. Czyzewski, private communication.
- [57] K.J. Eskola, Nucl. Phys. B **400**, 240 (1993).
- [58] K.J. Eskola, V.J. Kolhinen, and R. Vogt, Nucl. Phys. A **696**, 729 (2001).
- [59] D. Acosta *et al.* (CDF Collab.), Phys. Rev. D **65**, 052005 (2002).
- [60] M. Cacciari and P. Nason, hep-ph/0204025.
- [61] R.N. Cahn and J.D. Jackson, Phys. Rev. D **42**, 3690 (1990); G. Baur and L.G. Ferreira Filho, Nucl. Phys. A **518**, 786 (1990); M. Vidović, M. Greiner, C. Best, and G. Soff, Phys. Rev. C **47**, 2308 (1993); K. Hencken, D. Trautmann and G. Baur, Z. Phys. C **68**, 473 (1995).
- [62] A. Böhrer and M. Krawczyk, in Proc. of the International Conference on the Structure and Interactions of the Photon, *PHOTON 2001*, Ascona, Switzerland, September 2001, to be published in World Scientific, hep-ph/0203231.

- [63] R.V. Gavai *et al.*, Int. J. Mod. Phys. A **10** 3043 (1995); G.A. Schuler and R. Vogt, Phys. Lett. B **387**, 181 (1996).
- [64] V.P. Andreev, in Proc. of the International Conference on the Structure and Interactions of the Photon, *PHOTON 2001*, Ascona, Switzerland, September 2001, to be published in World Scientific.
- [65] J. Ohnemus, T.F. Walsh and P.M. Zerwas, Phys. Lett. B **328**, 369 (1994).
- [66] N. Kidonakis, E. Laenen, S. Moch and R. Vogt, Phys. Rev. D **64**, 114001 (2001).
- [67] R. Vogt, Z. Phys. C **71**, 475 (1996).
- [68] R. Vogt, hep-ph/0207359.
- [69] M. Villa (HERA-B Collab.), private communication.
- [70] A.J. Baltz, S.R. Klein and J. Nystrand, Phys. Rev. Lett. **89**, 012301 (2002).
- [71] C. Albajar *et al.*, Nucl. Phys. B **335**, 261 (1990).
- [72] C. Adler *et al.* (STAR Collab.), Phys. Rev. Lett. **87**, 112303 (2001).
- [73] C.G. Roldao and A.A. Natale, Phys. Rev. C **61**, 064907 (2000).

TABLES

A	AA		pA	
	$\sqrt{S_{NN}}$ (GeV)	\mathcal{L}_{AA} (cm ⁻² s ⁻¹)	$\sqrt{S_{NN}}$ (GeV)	\mathcal{L}_{pA} (cm ⁻² s ⁻¹)
RHIC				
O	250	9.8×10^{28}	250	1.2×10^{30}
Si	250	4.4×10^{28}	250	8×10^{29}
I	208	2.7×10^{27}	208	2×10^{29}
Au	200	2×10^{26}	200	6×10^{28}
LHC				
O	7000	1.6×10^{29}	9900	1.0×10^{31}
Ar	6300	4.3×10^{28}	9390	5.8×10^{30}
Pb	5500	4.2×10^{26}	8800	7.4×10^{29}

TABLE I. Luminosities and beam energies for AA and pA collisions at RHIC and LHC.

A	E_{beam} (GeV)	γ_L	AA		
			k_{max} (GeV)	E_{max} (TeV)	$\sqrt{S_{\text{max}}}$ (GeV)
RHIC					
O	125	133	12.7	2.31	66
Si	125	133	8.5	1.92	60
I	104	111	3.9	0.81	39
Au	100	106	3.2	0.66	35
LHC					
O	3500	3730	357	1820	1850
Ar	3150	3360	185	1080	1430
Pb	2750	2930	87.0	480	950
pA LHC					
O	4950	5270	435	3630	2610
Ar	4700	5000	276	2410	2130
Pb	4400	4690	139	1220	1500

TABLE II. Beam energies, E_{beam} , Lorentz factors, γ_L , photon cutoff energy in the center of mass frame, k_{max} , and in the nuclear rest frame, E_{max} , and equivalent nucleon-nucleon center of mass energy, $\sqrt{S_{\text{max}}}$, for AA collisions at RHIC and the LHC. Since the ion and proton beam energies are expected to be the same in pA and AA collisions at RHIC, we only distinguish the pA energies at LHC.

AA	$\sigma^{\text{dir}}(S^i = 1)$ (mb)	$\sigma^{\text{dir}}(\text{EKS98})$ (mb)	$\sigma^{\text{res}}(S^i = 1)$ (mb)	$\sigma^{\text{res}}(\text{EKS98})$ (mb)
RHIC				
O+O	0.067	0.068	0.0019	0.0019
Si+Si	0.30	0.31	0.0080	0.0083
I+I	8.96	9.74	0.199	0.206
Au+Au	24.8	27.4	0.530	0.550
LHC				
O+O	2.35	2.13	0.351	0.346
Ar+Ar	23.3	20.4	3.00	2.93
Pb+Pb	1790	1500	190.0	186.7

TABLE III. Direct and resolved $c\bar{c}$ photoproduction cross sections integrated over $b > 2R_A$ in peripheral AA collisions at RHIC and LHC.

AA	$\sigma^{\text{dir}}(S^i = 1)$ (μb)	$\sigma^{\text{dir}}(\text{EKS98})$ (μb)	$\sigma^{\text{res}}(S^i = 1)$ (μb)	$\sigma^{\text{res}}(\text{EKS98})$ (μb)
RHIC				
O+O	0.047	0.049	0.0031	0.0031
Si+Si	0.178	0.188	0.0116	0.0115
I+I	2.33	2.46	0.154	0.148
Au+Au	4.94	5.22	0.332	0.315
LHC				
O+O	11.9	11.4	2.93	2.93
Ar+Ar	107	102	22.2	22.6
Pb+Pb	718	686	121	126

TABLE IV. Direct and resolved $b\bar{b}$ photoproduction cross sections integrated over $b > 2R_A$ in peripheral AA collisions at RHIC and LHC.

pA	$c\bar{c}$		$b\bar{b}$	
	$\sigma^{\text{dir}}(S^i = 1)$ (μb)	$\sigma^{\text{res}}(S^i = 1)$ (μb)	$\sigma^{\text{dir}}(S^i = 1)$ (nb)	$\sigma^{\text{res}}(S^i = 1)$ (nb)
RHIC				
$p\text{O}$	2.68	0.081	2.34	0.154
$p\text{Si}$	7.29	0.213	5.79	0.378
$p\text{I}$	54.2	1.32	23.5	1.52
$p\text{Au}$	100	2.34	35.5	2.31
LHC				
$p\text{O}$	110	20.7	630	202
$p\text{Ar}$	485	83.9	2670	774
$p\text{Pb}$	7940	1190	40100	9910

TABLE V. Direct and resolved $c\bar{c}$ and $b\bar{b}$ photoproduction cross sections integrated over $b > r_p + R_A$ in pA collisions at RHIC and LHC.

AA	$c\bar{c}$		$b\bar{b}$	
	$N(S^i = 1)$	$N(\text{EKS98})$	$N(S^i = 1)$	$N(\text{EKS98})$
	RHIC			
O+O	6.75×10^6	6.94×10^6	4.88×10^3	5.10×10^3
Si+Si	1.36×10^7	1.41×10^7	8.35×10^3	8.73×10^3
I+I	2.47×10^7	2.69×10^7	6.70×10^3	7.06×10^3
Au+Au	5.07×10^6	5.60×10^6	1.06×10^3	1.10×10^3
	LHC			
O+O	4.15×10^8	3.80×10^8	2.29×10^6	2.20×10^6
Ar+Ar	1.13×10^9	9.98×10^8	5.58×10^6	5.37×10^6
Pb+Pb	8.29×10^8	7.05×10^8	3.58×10^5	3.46×10^5

TABLE VI. Total $c\bar{c}$ and $b\bar{b}$ photoproduction rates in peripheral AA collisions over a 10^6 s run at RHIC and LHC. The rates are based on Tables III and IV.

pA	$c\bar{c}$		$b\bar{b}$	
	$N(S^i = 1)$	$N(\text{EKS98})$	$N(S^i = 1)$	$N(\text{EKS98})$
	RHIC			
pO	3.30×10^6	3.30×10^6	2.99×10^3	2.99×10^3
pSi	6.00×10^6	6.00×10^6	4.93×10^3	4.93×10^3
pI	1.11×10^5	1.11×10^5	5.00×10^3	5.00×10^3
pAu	6.08×10^5	6.08×10^5	2.27×10^3	2.27×10^3
	LHC			
pO	1.32×10^9	1.32×10^9	8.32×10^6	8.32×10^6
pAr	3.11×10^9	3.11×10^9	1.88×10^7	1.88×10^7
pPb	6.70×10^9	6.70×10^9	3.69×10^7	3.69×10^7

TABLE VII. Total $c\bar{c}$ and $b\bar{b}$ photoproduction rates in pA collisions over a 10^6 s run at RHIC and LHC. The rates are based on Table V.

AA	$\sigma(S^i = 1)$ (mb)	$\sigma(\text{EKS98})$ (mb)	$\sigma(\text{EKS98}b)$ (mb)
	RHIC		
O+O	4.04	3.93	4.00
Si+Si	8.54	8.22	8.42
I+I	22.6	21.6	22.3
Au+Au	33.1	31.6	32.6
	LHC		
O+O	113	93.2	104
Ar+Ar	426	323	379
Pb+Pb	1090	714	948

TABLE VIII. Total $c\bar{c}$ hadroproduction cross sections integrated over $b > 2R_A$ in peripheral AA collisions at RHIC and LHC.

AA	$N(S^i = 1)$	$N(\text{EKS98})$	$N(\text{EKS98}b)$
RHIC			
O+O	3.96×10^8	3.85×10^8	3.92×10^8
Si+Si	3.76×10^8	3.62×10^8	3.70×10^8
I+I	6.10×10^7	5.84×10^7	6.02×10^7
Au+Au	6.62×10^6	6.33×10^6	6.52×10^6
LHC			
O+O	1.74×10^{10}	1.44×10^{10}	1.61×10^{10}
Ar+Ar	1.83×10^{10}	1.39×10^{10}	1.63×10^{10}
Pb+Pb	4.57×10^8	3.00×10^8	3.98×10^8

TABLE IX. Total $c\bar{c}$ hadroproduction rates in peripheral AA collisions at RHIC and LHC with a 10^6 s run. The rates are based on Table VIII.

AA	$\sigma(S^i = 1)$ (μb)	$\sigma(\text{EKS98})$ (μb)	$\sigma(\text{EKS98}b)$ (μb)
RHIC			
O+O	22.7	24.1	23.3
Si+Si	47.9	51.7	49.5
I+I	111	127	117
Au+Au	154	183	167
LHC			
O+O	2490	2260	2390
Ar+Ar	9110	7930	8600
Pb+Pb	21700	17500	20200

TABLE X. Total $b\bar{b}$ hadroproduction cross sections integrated over $b > 2R_A$ in peripheral AA collisions.

AA	$N(S^i = 1)$	$N(\text{EKS98})$	$N(\text{EKS98}b)$
RHIC			
O+O	2.22×10^6	2.36×10^6	2.27×10^6
Si+Si	2.11×10^6	2.27×10^6	2.18×10^6
I+I	3.01×10^5	3.43×10^5	3.16×10^5
Au+Au	3.17×10^4	3.67×10^4	3.34×10^4
LHC			
O+O	3.84×10^8	3.48×10^8	3.68×10^8
Ar+Ar	3.92×10^8	3.41×10^8	3.70×10^8
Pb+Pb	9.11×10^6	7.35×10^6	8.48×10^6

TABLE XI. Total $b\bar{b}$ hadroproduction rates in peripheral AA collisions with a 10^6 s run at RHIC and LHC. The rates are based on Table X.

pA	$c\bar{c}$		$b\bar{b}$	
	$\sigma(S^i = 1)$ (mb)	$\sigma(\text{EKS98})$ (mb)	$\sigma(S^i = 1)$ (μb)	$\sigma(\text{EKS98})$ (μb)
RHIC				
$p\text{O}$	4.19	4.14	23.7	24.4
$p\text{Si}$	7.33	7.21	41.5	43.1
$p\text{I}$	26.2	25.8	131	139
$p\text{Au}$	38.6	38.1	187	201
LHC				
$p\text{O}$	153	138	3740	3540
$p\text{Ar}$	368	318	8850	8180
$p\text{Pb}$	1820	1460	43000	38200

TABLE XII. Total $c\bar{c}$ and $b\bar{b}$ hadroproduction cross sections in minimum bias (all b) pA collisions at RHIC and LHC.

pA	$c\bar{c}$		$b\bar{b}$	
	$N(S^i = 1)$	$N(\text{EKS98})$	$N(S^i = 1)$	$N(\text{EKS98})$
RHIC				
$p\text{O}$	5.02×10^9	4.96×10^9	2.85×10^7	2.92×10^7
$p\text{Si}$	5.86×10^9	5.77×10^9	3.32×10^7	3.45×10^7
$p\text{I}$	5.25×10^9	5.17×10^9	2.62×10^7	2.79×10^7
$p\text{Au}$	2.32×10^9	2.28×10^9	1.12×10^7	1.20×10^7
LHC				
$p\text{O}$	1.53×10^{12}	1.39×10^{12}	3.75×10^{10}	3.57×10^{10}
$p\text{Ar}$	2.01×10^{12}	1.75×10^{12}	4.87×10^{10}	4.50×10^{10}
$p\text{Pb}$	1.35×10^{12}	1.07×10^{12}	3.18×10^{10}	2.82×10^{10}

TABLE XIII. Total $c\bar{c}$ and $b\bar{b}$ hadroproduction rates in minimum bias pA collisions over a 10^6 s run at RHIC and LHC. The rates are based on Table XII.

AA	all $c\bar{c}$			$M > 2m_D$		
	σ^{dir} (nb)	$\sigma^{1\text{-res}}$ (nb)	$\sigma^{2\text{-res}}$ (nb)	σ^{dir} (nb)	$\sigma^{1\text{-res}}$ (nb)	$\sigma^{2\text{-res}}$ (nb)
RHIC						
O+O	4.64	0.08	0.0020	1.65	0.022	0.00039
Si+Si	32.0	0.49	0.013	10.8	0.125	0.0023
I+I	1320	10.7	0.345	288	1.18	0.027
Au+Au	3650	22.2	0.786	601	1.37	0.035
LHC						
O+O	236	11.7	0.24	128	6.01	0.10
Ar+Ar	4530	210.0	4.36	2410	105	1.76
Pb+Pb	1110000	45000	951	565000	21400	352

TABLE XIV. Two photon $c\bar{c}$ cross sections in peripheral AA collisions at RHIC and LHC, integrated over $b > 2R_A$.

AA	all $b\bar{b}$			$M > 2m_B$		
	σ^{dir} (pb)	$\sigma^{1\text{-res}}$ (pb)	$\sigma^{2\text{-res}}$ (pb)	σ^{dir} (pb)	$\sigma^{1\text{-res}}$ (pb)	$\sigma^{2\text{-res}}$ (pb)
RHIC						
O+O	0.268	0.0018	0.00038	0.194	0.0010	0.00029
Si+Si	0.923	0.0031	0.00083	0.582	0.0013	0.00046
LHC						
O+O	285	31.7	3.08	262.6	28.9	2.62
Ar+Ar	4890	491.0	49.3	4480	444	41.7
Pb+Pb	943000	75000	8260	855000	66800	6820

TABLE XV. Two photon $b\bar{b}$ cross sections in peripheral AA collisions at RHIC and LHC, integrated over $b > 2R_A$.

AA	all $Q\bar{Q}$		$M > 2m_H$	
	$N(c\bar{c})$	$N(b\bar{b})$	$N(c\bar{c})$	$N(b\bar{b})$
RHIC				
O+O	4.62×10^2	2.65×10^{-2}	1.64×10^2	1.91×10^{-2}
Si+Si	1.43×10^3	4.08×10^{-2}	4.81×10^2	2.57×10^{-2}
I+I	3.61×10^3	-	7.81×10^2	-
Au+Au	7.36×10^2	-	1.21×10^2	-
LHC				
O+O	3.97×10^4	5.11×10^1	2.15×10^4	4.71×10^1
Ar+Ar	2.04×10^5	2.33×10^2	1.08×10^5	2.13×10^2
Pb+Pb	4.84×10^5	4.41×10^2	2.47×10^5	3.90×10^2

TABLE XVI. Total $c\bar{c}$ and $b\bar{b}$ two-photon rates in peripheral AA collisions over a 10^6 s run at RHIC and LHC. The rates are based on Tables XIV and XV.

FIGURES

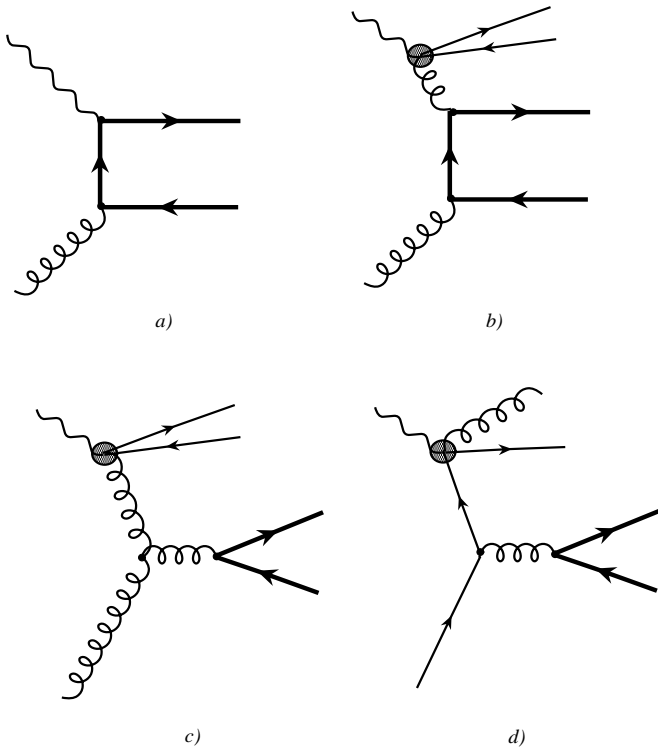


FIG. 1. Feynman diagrams for heavy quark photoproduction for (a) direct and (b)-(d) resolved photons. The crossed diagrams for (a) and (b) are not shown.

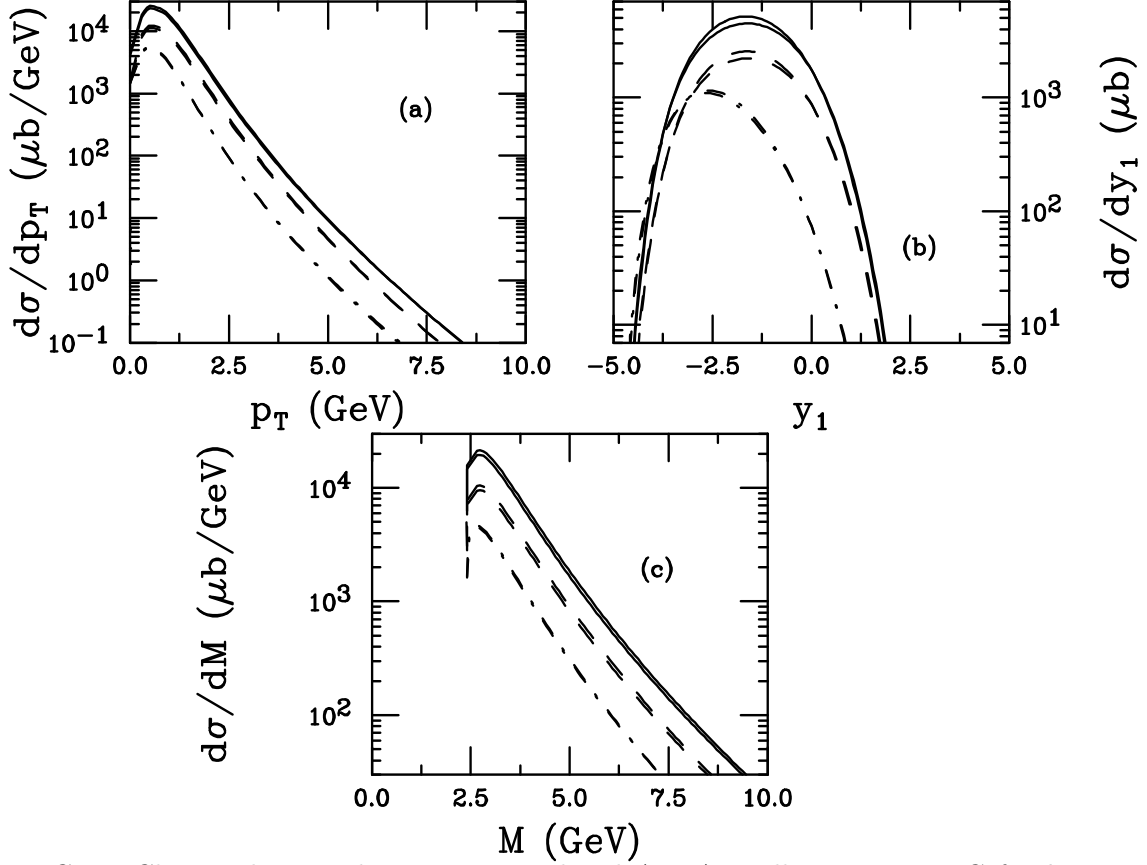


FIG. 2. Charm photoproduction in peripheral Au+Au collisions at RHIC for $b > 2R_A$. The single c quark p_T (a) and rapidity (b) distributions are shown along with the $c\bar{c}$ pair invariant mass (c). The direct (dashed), resolved (dot-dashed), and the sum of the two (solid) are shown. The direct contribution is divided by two to distinguish it from the total while the resolved contribution is multiplied by ten. There are two curves for each contribution: $S^i = 1$ and EKS98. At this energy, the curves are almost indistinguishable but the curves with shadowing are somewhat higher, especially at negative rapidities. In the rapidity distributions, the photon is coming from the left.

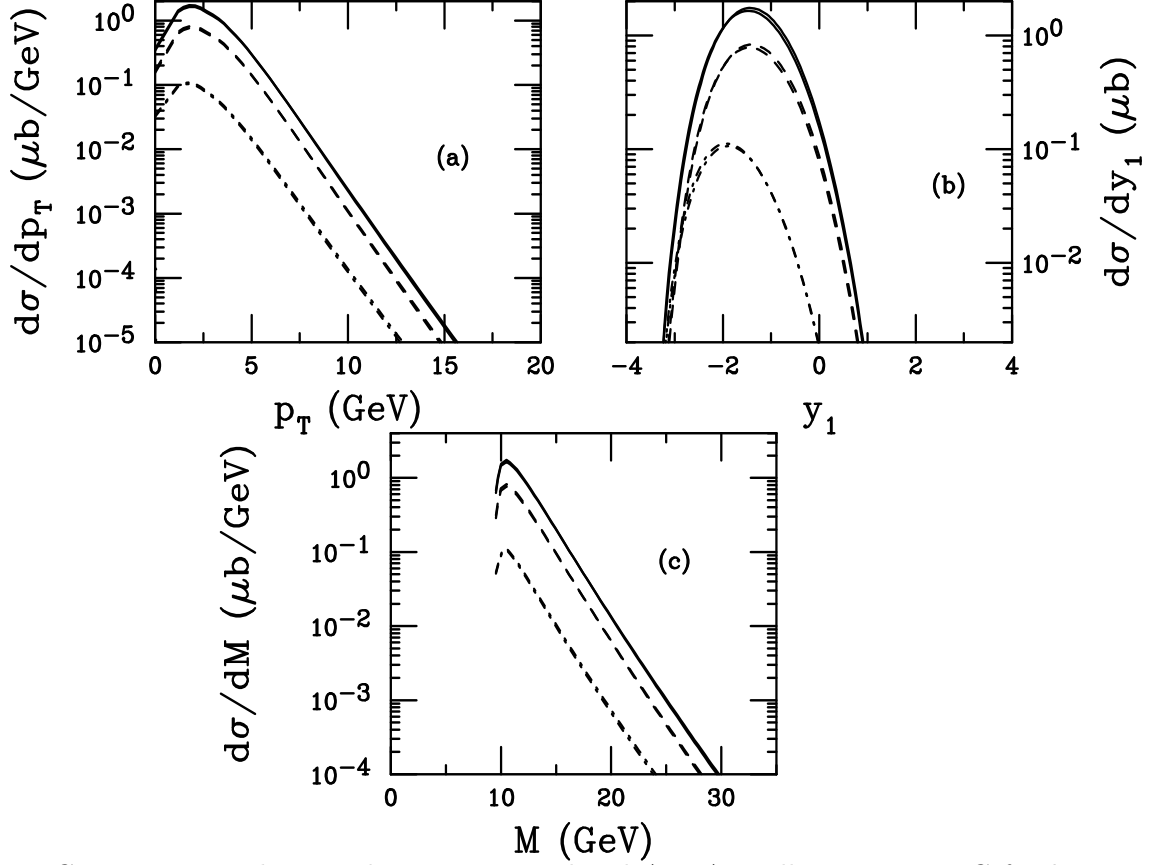


FIG. 3. Bottom photoproduction in peripheral Au+Au collisions at RHIC for $b > 2R_A$. The single b quark p_T (a) and rapidity (b) distributions are shown along with the $b\bar{b}$ pair invariant mass (c). The direct (dashed), resolved (dot-dashed), and the sum of the two (solid) are shown. The direct contribution is divided by two to distinguish it from the total. There are two curves for each contribution: $S^i = 1$ and EKS98. At this energy, the curves are almost indistinguishable. In the rapidity distributions, the photon is coming from the left.

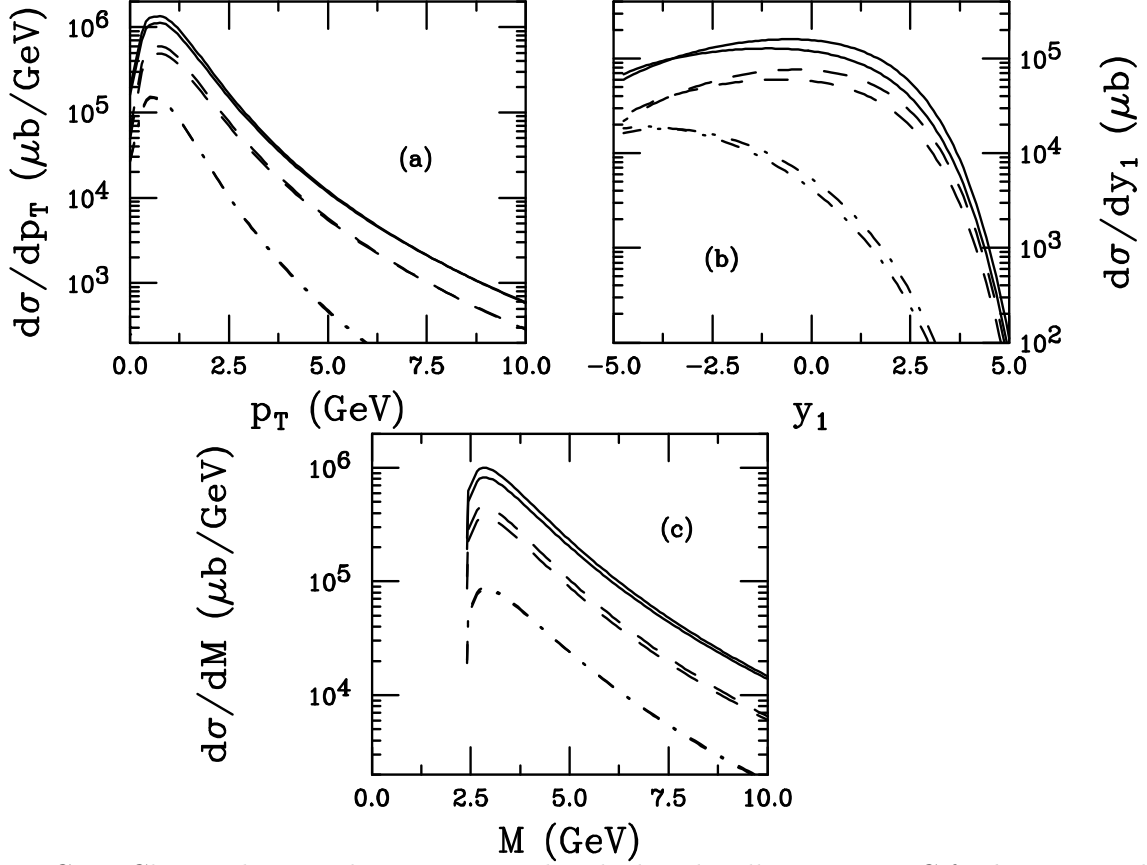


FIG. 4. Charm photoproduction in peripheral Pb+Pb collisions at LHC for $b > 2R_A$. The single c quark p_T (a) and rapidity (b) distributions are shown along with the $c\bar{c}$ pair invariant mass (c). The direct (dashed), resolved (dot-dashed), and the sum of the two (solid) are shown. The direct contribution is divided by two to distinguish it from the total. There are two curves for each contribution: $S^i = 1$ and EKS98. The unshaded curves are higher than the shadowed, particularly at large rapidities. In the rapidity distributions, the photon is coming from the left.

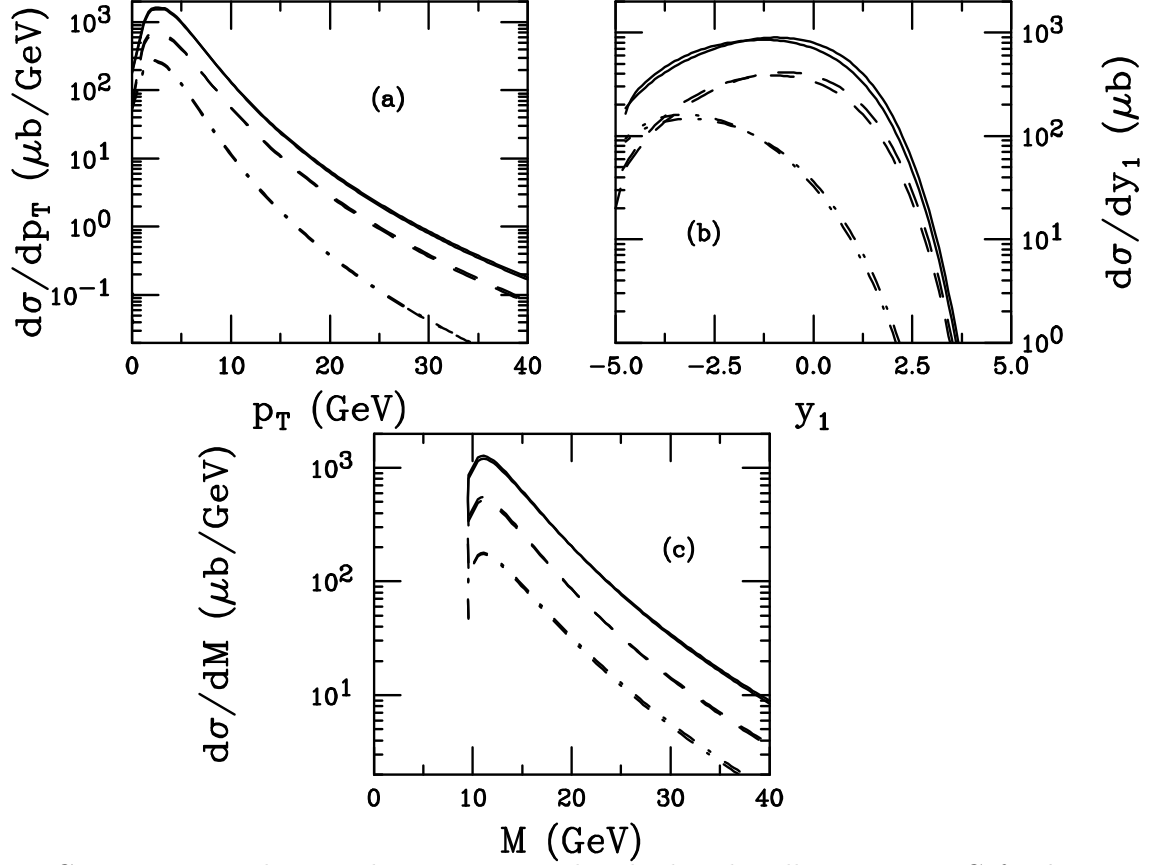


FIG. 5. Bottom photoproduction in peripheral Pb+Pb collisions at LHC for $b > 2R_A$. The single b quark p_T (a) and rapidity (b) distributions are shown along with the $b\bar{b}$ pair invariant mass (c). The direct (dashed), resolved (dot-dashed), and the sum of the two (solid) are shown. The direct contribution is divided by two to distinguish it from the total. There are two curves for each contribution: $S^i = 1$ and EKS98. The unshaded curves are higher than the shaded. In the rapidity distributions, the photon is coming from the left.

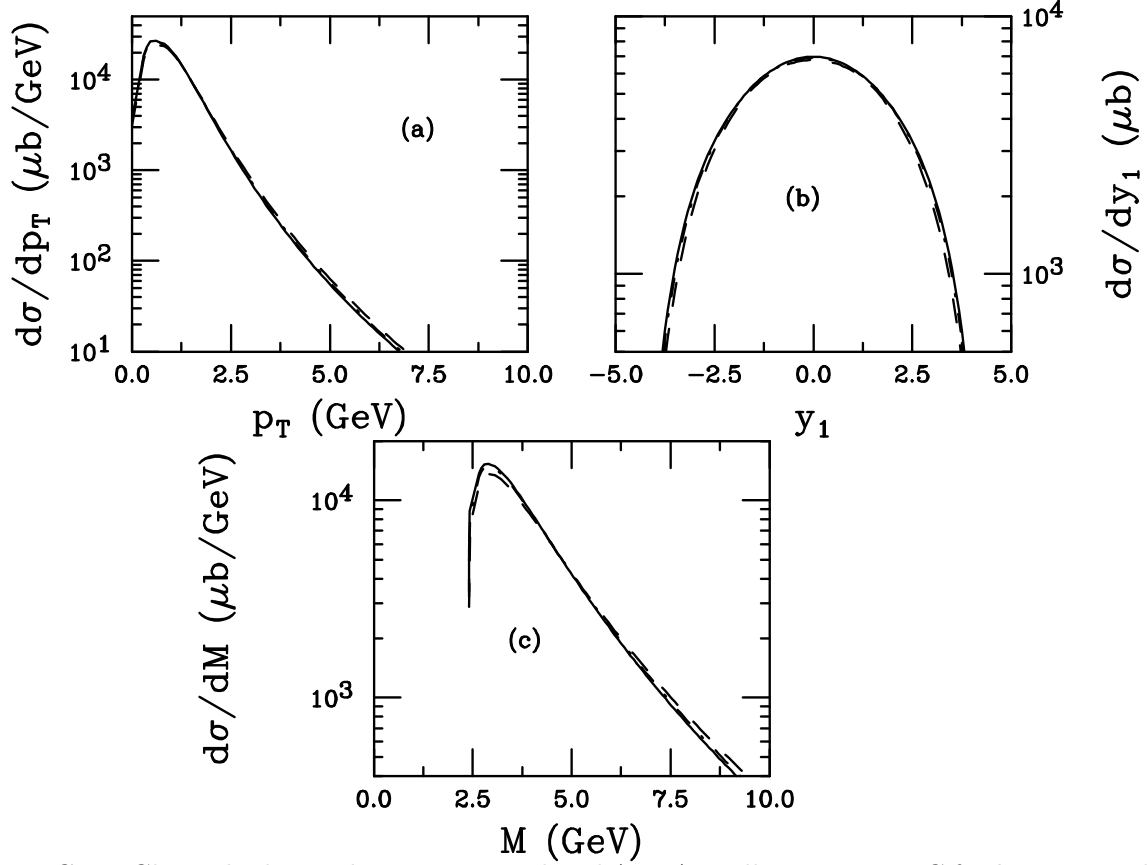


FIG. 6. Charm hadroproduction in peripheral Au+Au collisions at RHIC for $b > 2R_A$. The single c quark p_T (a) and rapidity (b) distributions are shown along with the $c\bar{c}$ pair invariant mass (c). The curves are $S^i = 1$ (solid), EKS98 (dashed), and EKS98b (dot-dashed). At this energy, the three curves are almost indistinguishable.

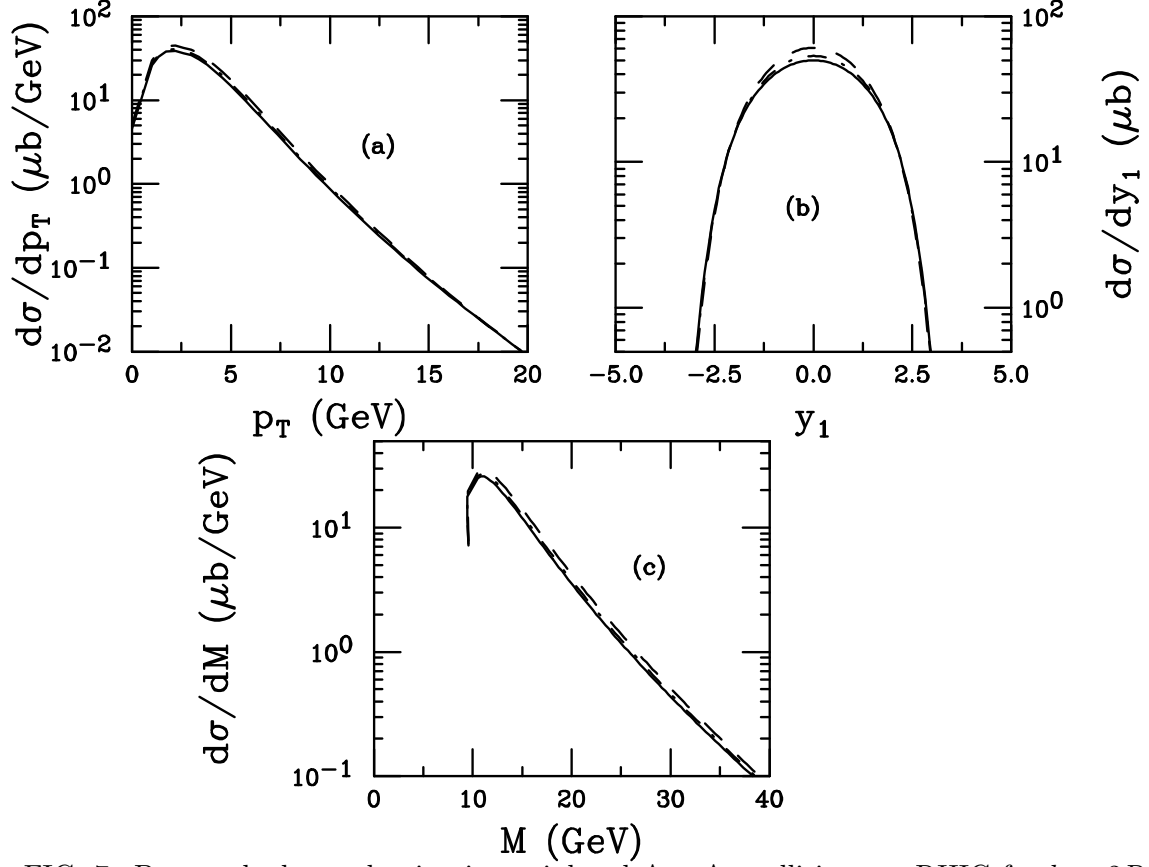


FIG. 7. Bottom hadroproduction in peripheral Au+Au collisions at RHIC for $b > 2R_A$. The single b quark p_T (a) and rapidity (b) distributions are shown along with the $b\bar{b}$ pair invariant mass (c). The curves are $S^i = 1$ (solid), EKS98 (dashed), and EKS98b (dot-dashed).

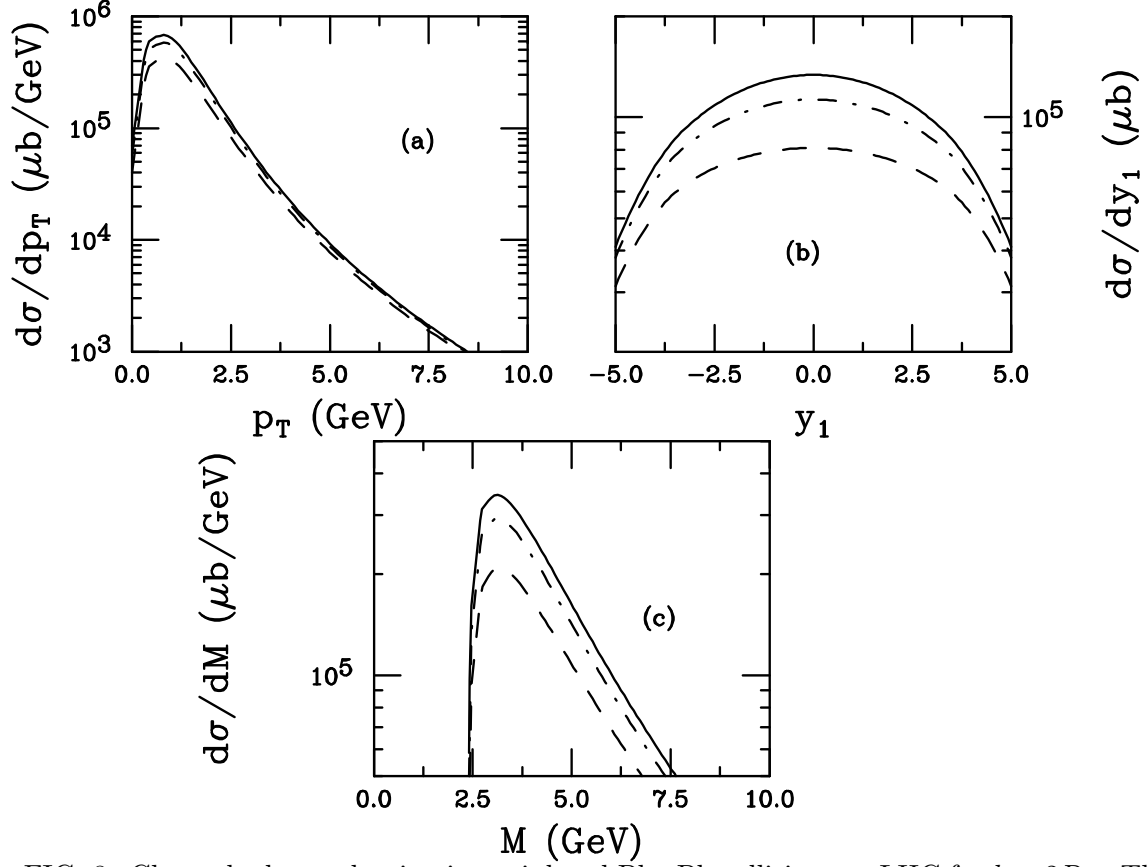


FIG. 8. Charm hadroproduction in peripheral Pb+Pb collisions at LHC for $b > 2R_A$. The single c quark p_T (a) and rapidity (b) distributions are shown along with the $c\bar{c}$ pair invariant mass (c). The curves are $S^i = 1$ (solid), EKS98 (dashed), and EKS98b (dot-dashed).

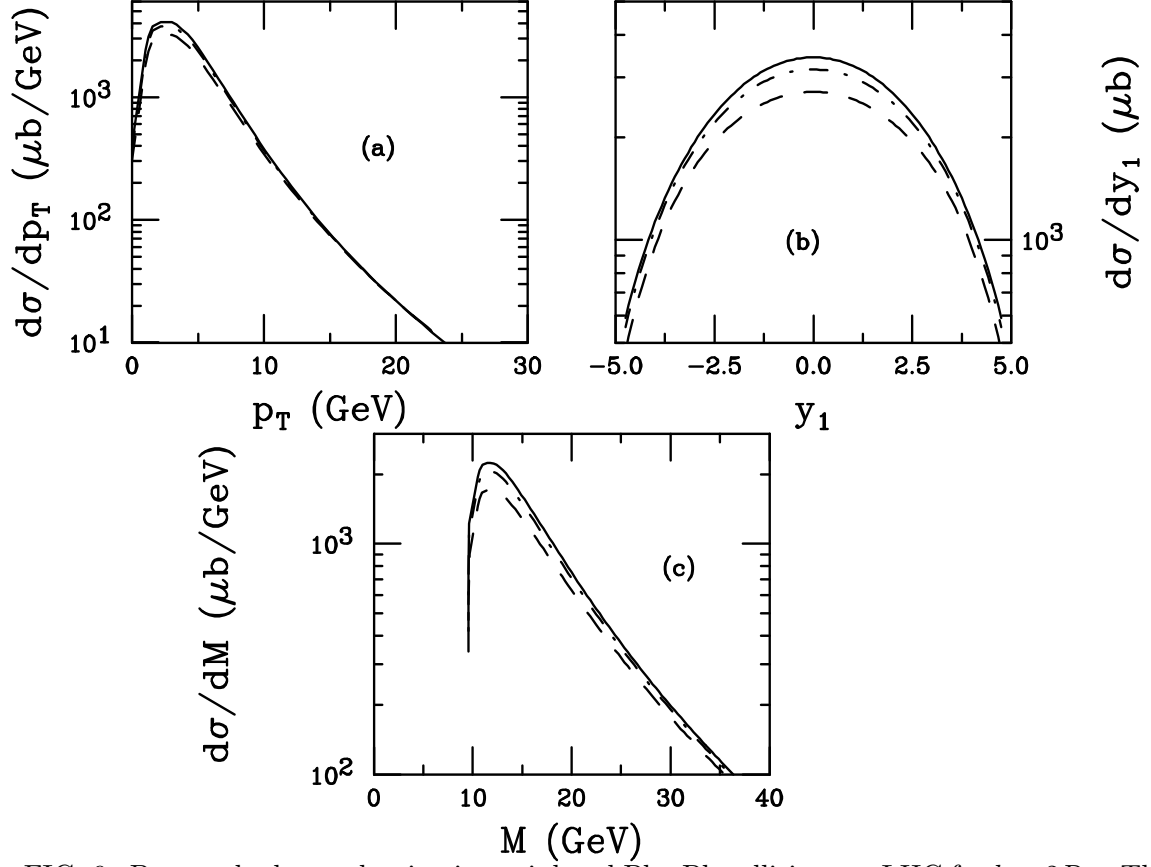


FIG. 9. Bottom hadroproduction in peripheral Pb+Pb collisions at LHC for $b > 2R_A$. The single b quark p_T (a) and rapidity (b) distributions are shown along with the $b\bar{b}$ pair invariant mass (c). The curves are $S^i = 1$ (solid), EKS98 (dashed), and EKS98b (dot-dashed).

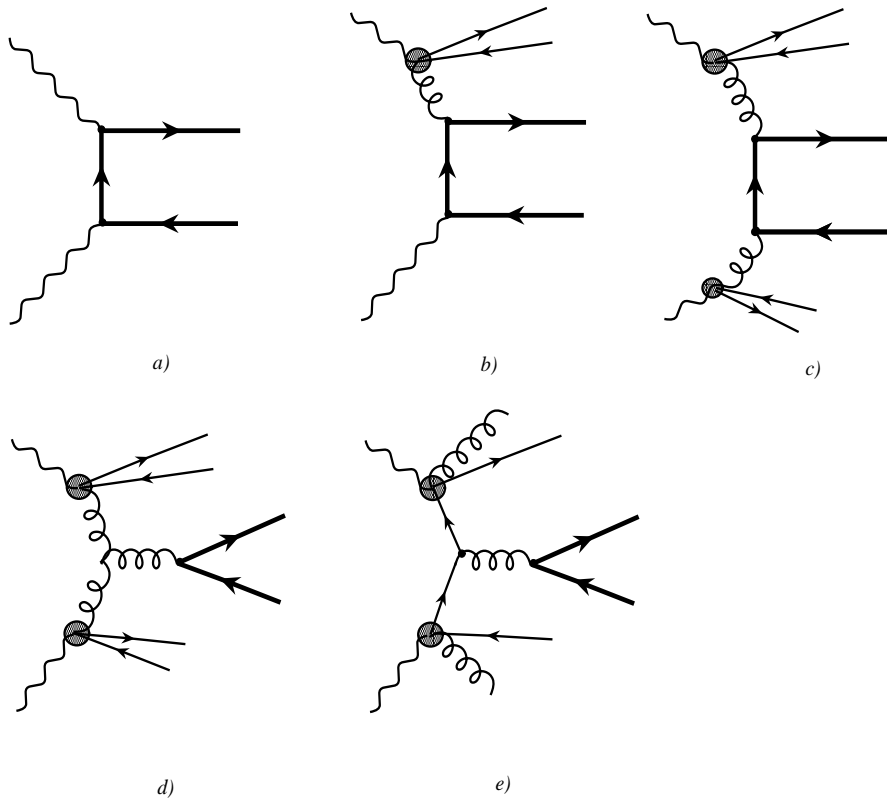


FIG. 10. Feynman diagrams for two-photon production of heavy quarks in (a) direct, (b) single-resolved, and (c)-(e) double-resolved photons. The crossed diagrams for (a) through (c) are not shown.

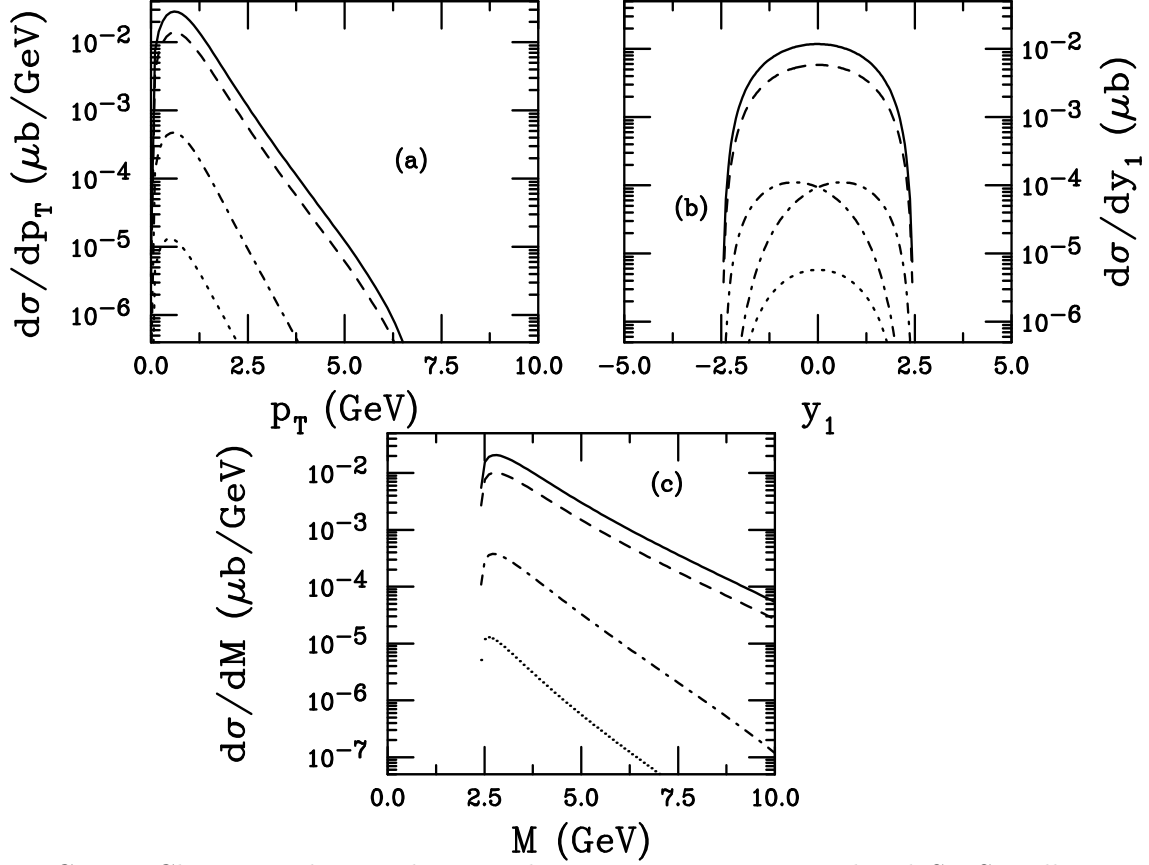


FIG. 11. Charm production by two-photon processes in peripheral Si+Si collisions at RHIC. The results are shown for all pairs with no mass cut. The single c quark p_T (a) and rapidity (b) distributions are shown along with the $c\bar{c}$ pair invariant mass (c). The solid curve is the sum of all contributions: σ^{dir} (dashed), $\sigma^{1\text{-res}}$ (dot-dashed), and $\sigma^{2\text{-res}}$ (dotted). The direct contribution is divided by two to facilitate comparison. Since either photon can be resolved, the single-resolved rapidity distribution is reflected around $y_1 = 0$ to account for both sources.

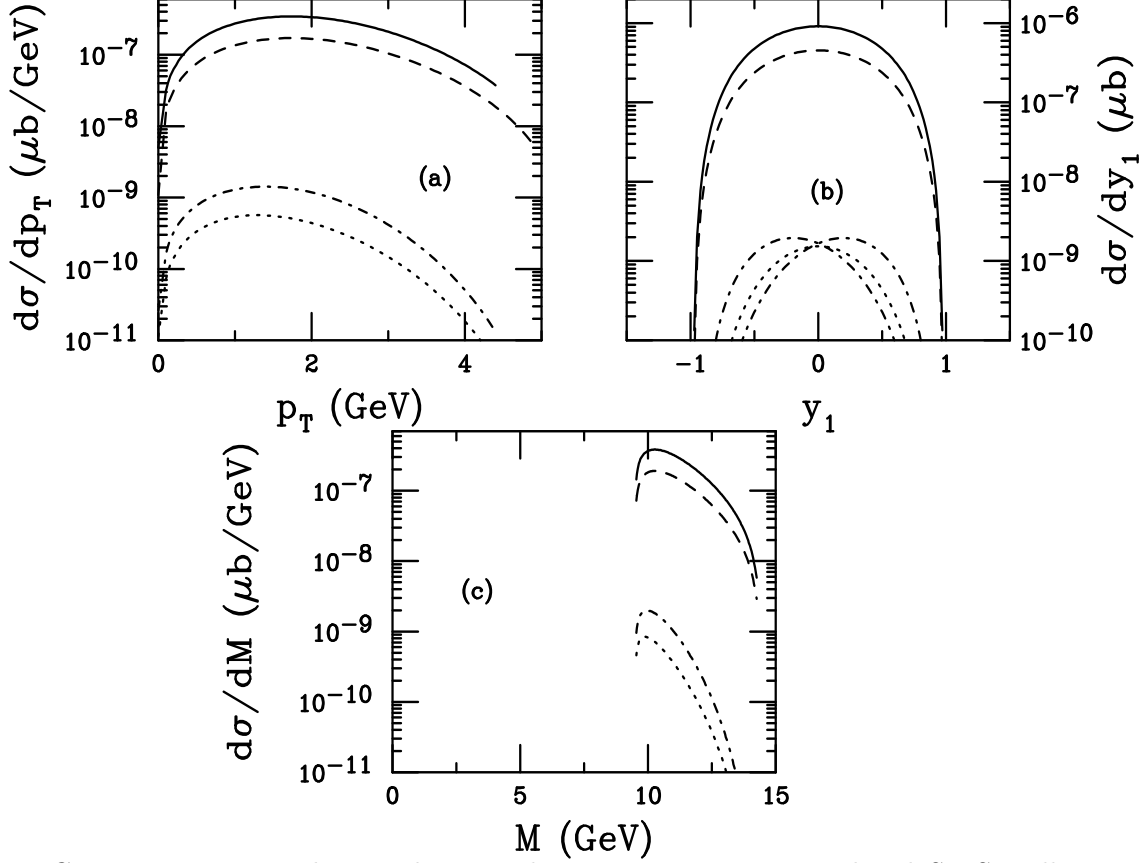


FIG. 12. Bottom production by two-photon processes in peripheral Si+Si collisions at RHIC. The results are shown for all pairs with no mass cut. The single b quark p_T (a) and rapidity (b) distributions are shown along with the $b\bar{b}$ pair invariant mass (c). The solid curve is the sum of all contributions: σ^{dir} (dashed), $\sigma^{1\text{-res}}$ (dot-dashed), and $\sigma^{2\text{-res}}$ (dotted). The direct contribution is divided by two to facilitate comparison. Since either photon can be resolved, the single-resolved rapidity distribution is reflected around $y_1 = 0$ to account for both sources.

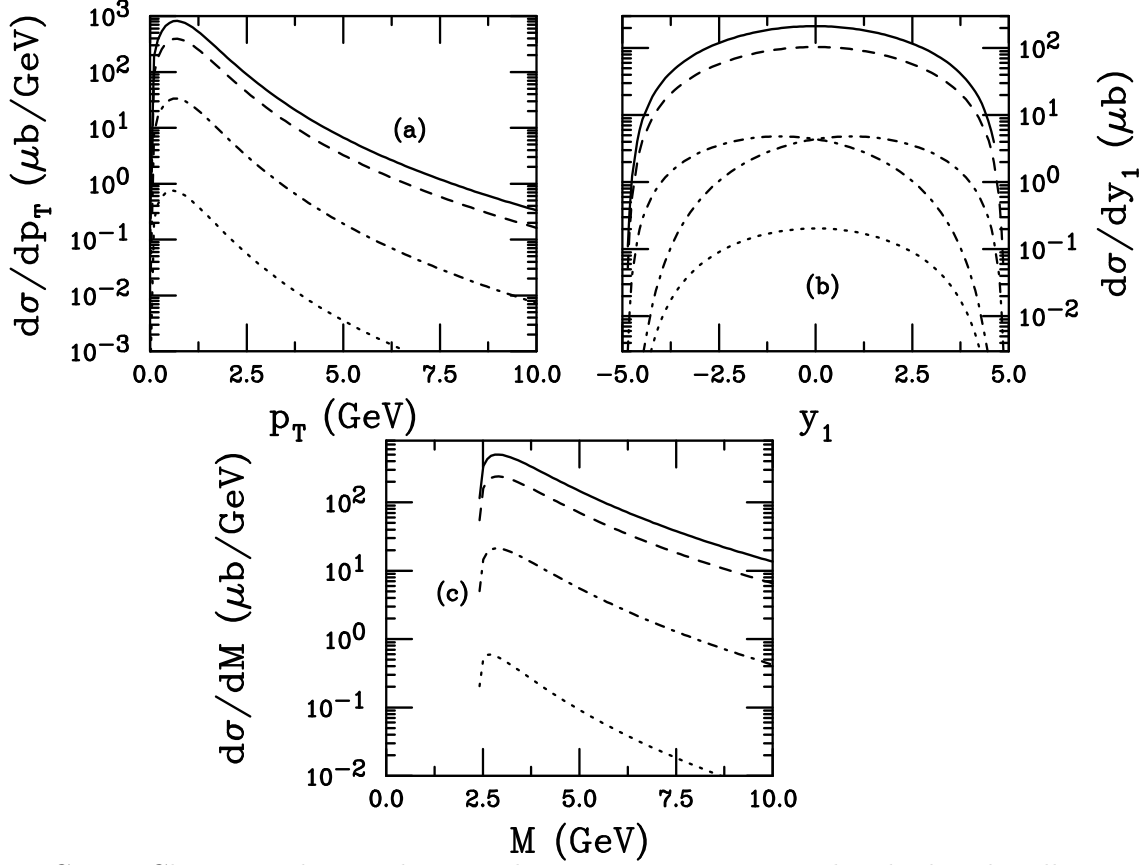


FIG. 13. Charm production by two-photon processes in peripheral Pb+Pb collisions at LHC. The results are shown for all pairs with no mass cut. The single c quark p_T (a) and rapidity (b) distributions are shown along with the $c\bar{c}$ pair invariant mass (c). The solid curve is the sum of all contributions: σ^{dir} (dashed), $\sigma^{1\text{-res}}$ (dot-dashed), and $\sigma^{2\text{-res}}$ (dotted). The direct contribution is divided by two to facilitate comparison. Since either photon can be resolved, the single-resolved rapidity distribution is reflected around $y_1 = 0$ to account for both sources.

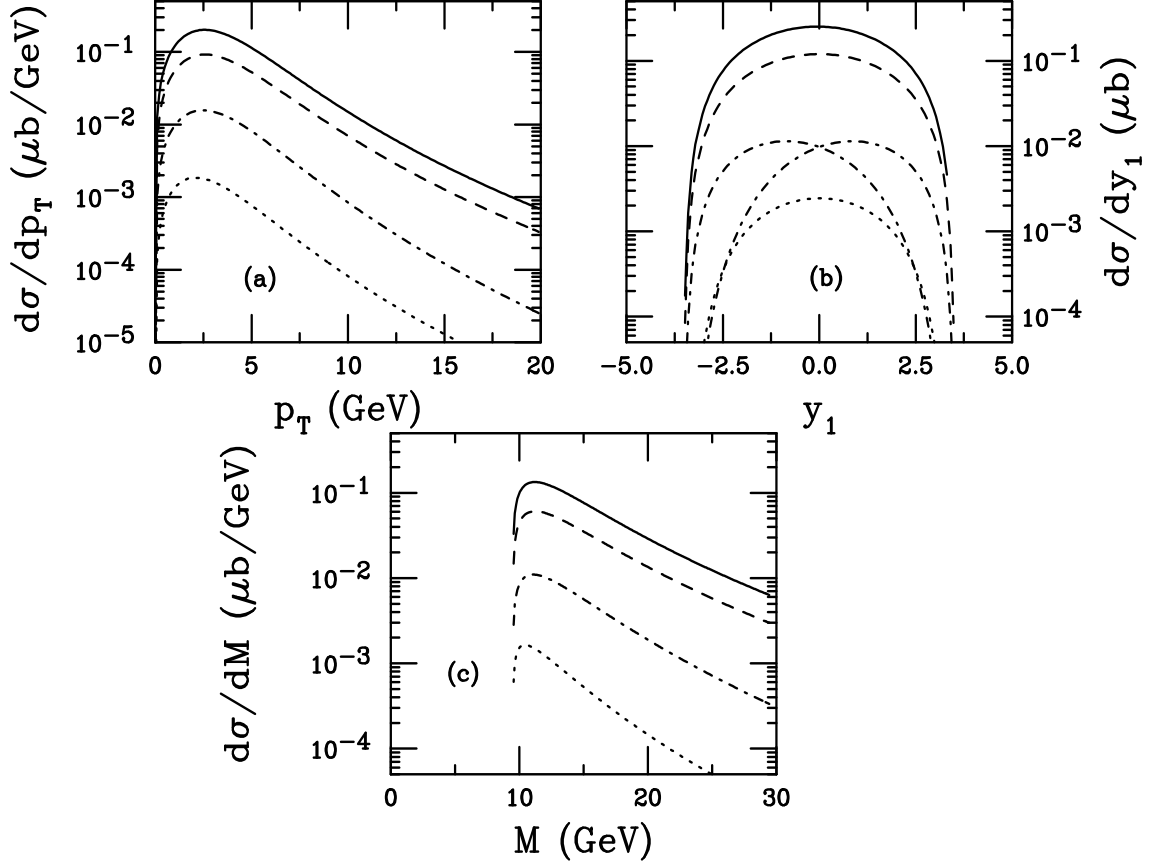


FIG. 14. Bottom production by two-photon processes in peripheral Pb+Pb collisions at LHC. The results are shown for all pairs with no mass cut. The single b quark p_T (a) and rapidity (b) distributions are shown along with the $b\bar{b}$ pair invariant mass (c). The solid curve is the sum of all contributions: σ^{dir} (dashed), $\sigma^{1\text{-res}}$ (dot-dashed), and $\sigma^{2\text{-res}}$ (dotted). The direct contribution is divided by two to facilitate comparison. Since either photon can be resolved, the single-resolved rapidity distribution is reflected around $y_1 = 0$ to account for both sources.

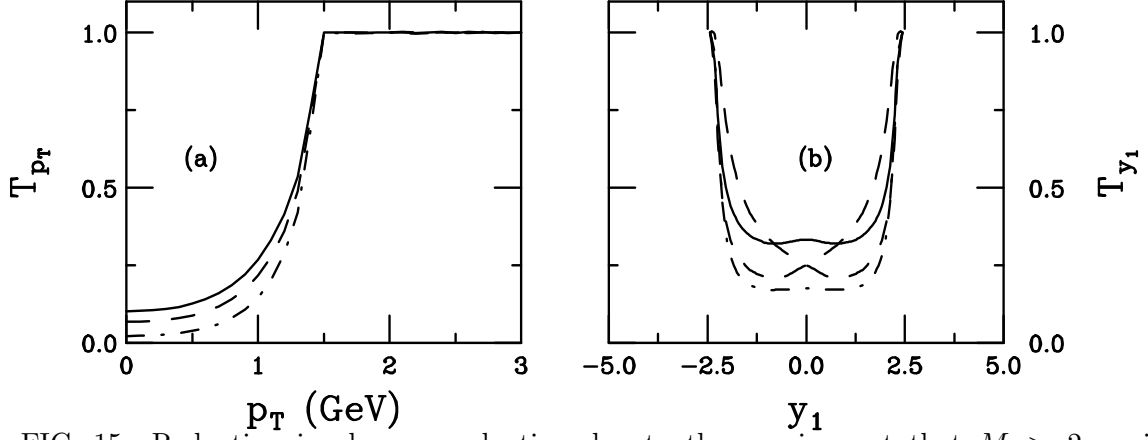


FIG. 15. Reduction in charm production due to the requirement that $M > 2m_D$ in two-photon production in peripheral Si+Si collisions at RHIC. The ratio of the cross section above threshold relative to the total cross section is shown as a function of p_T (a) and y_1 (b) for σ^{dir} (solid), $\sigma^{1\text{-res}}$ (dashed) and $\sigma^{2\text{-res}}$ (dot-dashed). Since either photon can be resolved, the single-resolved rapidity ratio is reflected around $y_1 = 0$ to account for both sources.

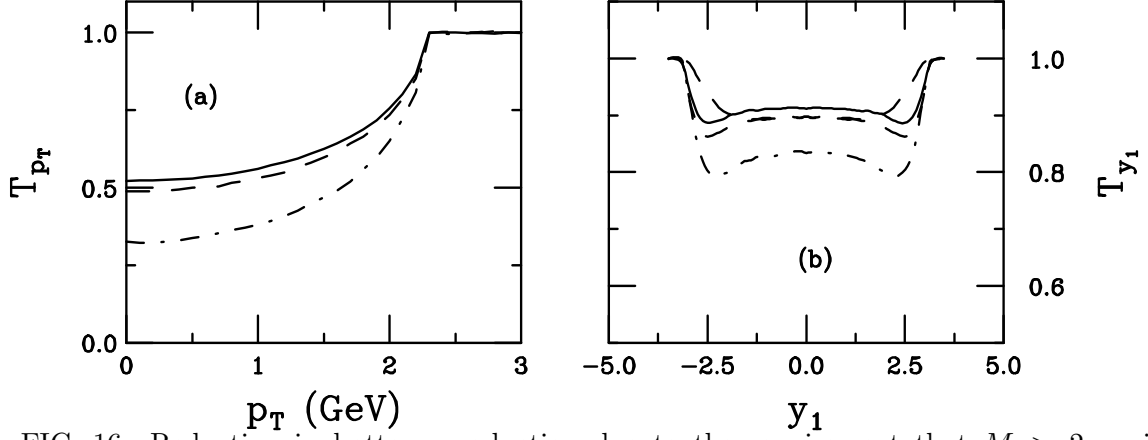


FIG. 16. Reduction in bottom production due to the requirement that $M > 2m_B$ in two-photon production in peripheral Pb+Pb collisions at LHC. The ratio of the cross section above threshold relative to the total cross section is shown as a function of p_T (a) and y_1 (b) for σ^{dir} (solid), $\sigma^{1\text{-res}}$ (dashed) and $\sigma^{2\text{-res}}$ (dot-dashed). Since either photon can be resolved, the single-resolved rapidity ratio is reflected around $y_1 = 0$ to account for both sources.

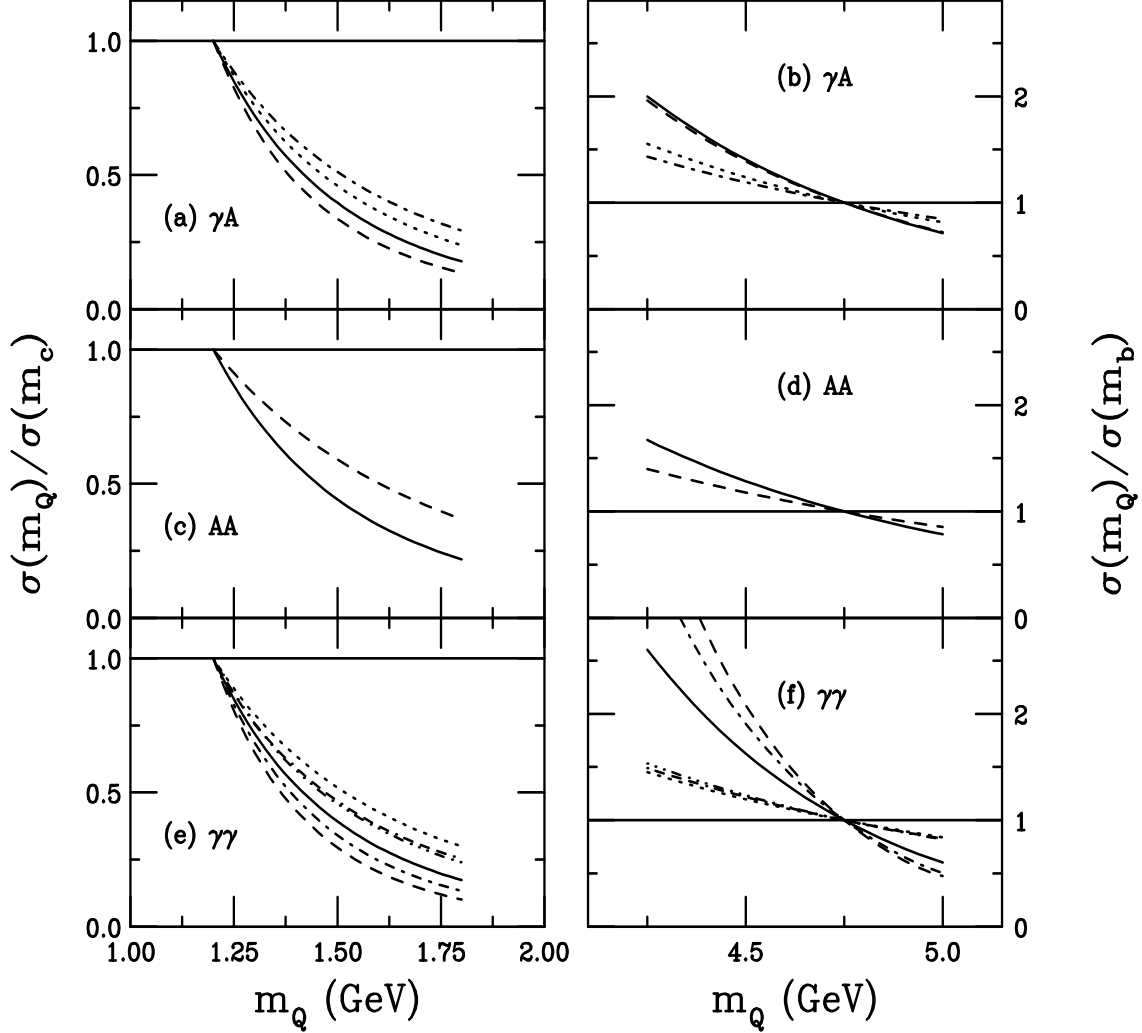


FIG. 17. The quark-mass dependence of our calculated cross sections. The left side is for charm, normalized to the cross sections with $m_c = 1.2$ GeV while the right side is for bottom, normalized to cross sections with $m_b = 4.75$ GeV. The RHIC results are for Si+Si interactions while the LHC results are for Pb+Pb interactions. The photoproduction ratios in (a) and (b) are for direct (solid–RHIC; dot-dashed–LHC) and resolved (dashed–RHIC; dotted–LHC) production. The hadroproduction results at RHIC and LHC are given by the solid and dashed curves respectively in (c) and (d). The two-photon ratios in (e) and (f) are for σ^{dir} (solid–RHIC; dotted–LHC), $\sigma^{1-\text{res}}$ (dashed–RHIC; dot-dot-dot-dashed–LHC) and $\sigma^{2-\text{res}}$ (dot-dashed–RHIC; dot-dash-dash-dashed–LHC).